IDO/77.3.1

FINAL: VOLUME 77-15

THREE DIMENSIONAL MAGNETOTELLURIC MODELING

Gerald W. Hohmann

and

Sam C. Ting

July 1978

Work performed under Contract No. EY-76-S-07-1601

EARTH SCIENCE LABORATORY
University of Utah Research Institute
Salt Lake City, Utah

Prepared for
U.S. Department of Energy
Division of Geothermal Energy

NOTICE

This report was prepared to document work sponsored by the United States Government. Neither the United States nor its agent, the United States Department of Energy, nor any Federal employees, nor any of their contractors, subcontractors or their employees, makes any warranty, express or implied, or assumes any legal liability or responsibility for the accuracy, completeness, or usefulness of any information, apparatus, product or process disclosed, or represents that its use would not infringe privately owned rights.

NOTICE

Reference to a company or product name does not imply approval or recommendation of the product by the University of Utah Research Institute or the U.S. Department of Energy to the exclusion of others that may be suitable.

CONTENTS

ABSTRACT

We have refined a three-dimensional (3D) volume integral equation solution, and have adapted it to magnetotelluric (MT) modeling. The refinement, incorporating an integro-difference scheme, increases the accuracy somewhat without increasing the computer time. Utilizing the two symmetry planes for a plane wave source decreases the computer storage by a factor of 8 and greatly reduces the computer time.

Convergence checks and comparisons with other solutions show that our results are valid. Because of space charges at resistivity boundaries, low-frequency 3D responses are much different from 1D and 2 D responses. Hence 3D models are required for interpreting MT data in the complex geothermal environment.

INTRODUCTION

Electrical geophysical techniques are essential in geothermal exploration and assessment. Because a convective hydrothermal system modifies the electrical conduction properties of rocks, surface electrical methods provide a picture of the subsurface --- if the data can be interpreted accurately.

The magnetotelluric (MT) method is one of the most widely used electrical prospecting techniques in geothermal work due to its capability for deep exploration. In spite of its promise, however, the MT method has been severely hampered by a lack of interpretation capability. Inappropriate one-dimensional (1D) and two-dimensional (2D) interpretation models are used because the necessary three-dimensional (3D) models are not available. These simple interpretation algorithms are useful for exploration in large sedimentary basins where 1D and 2D models apply. However, the results can be quite misleading in most geothermal exploration where the earth is three-dimensional and the TE and TM modes do not separate.

There are two basic approaches to numerical modeling: (1) differential equation (DE) and (2) integral equation (IE). Both methods are useful and necessary. Differential equation solutions are easier to set up, and they result in large banded matrices. Because the entire earth is modeled on a grid, DE methods are preferable for modeling complex geology. Integral equation formulations involve more difficult mathematics, but their advantage is that unknown fields must be found only in anomalous regions. Thus, integral equation solutions are less expensive for simulating the response of one or a few small bodies and hence are more useful for evaluating field

techniques, for designing surveys, and for generating catalogs of interpretation curves.

We have refined and adapted an integral equation solution (Hohmann, 1975) so that it can be used to simulate the MT response of a 3D body in the earth. The body is replaced by polarization currents which depend on the difference between the conductivity of the body and that of the surrounding earth. The resulting volume integral equation is reduced to a matrix equation by the method of moments (Harrington, 1968). After the matrix equation is solved for the polarization current, the electric and magnetic fields at the surface of the earth can be calculated using half-space dyadic Green's functions.

In this work we have re-formulated the integral equation solution using the vector-scalar potential approach with derivatives approximated by differences (Harrington, 1968) to improve convergence. Magnetotelluric modeling is easier than our previous controlled-source EM modeling (Hohmann, 1975) because there are two symmetry planes for a prismatic body. Hence the computer time is greatly reduced. The change to a plane wave source is trivial.

This report documents the theoretical solution and discusses results for initial models. Most of our effort thus far has been to improve the accuracy of the 3D solution and to verify the results. We have emphasized convergence checks and comparisons with 2D models and have made a few calculations on a surface grid.

INTEGRAL EQUATION FORMULATION

Consider the configuration shown in Figure 1. The earth is taken to be a half-space of conductivity σ_1, except for a rectangular inhomogeneity having conductivity σ_2. Relevant dimensions are depth D, width W, strike length L, and depth extent DE. The earth is excited by impressed magnetic or electric currents, which are denoted by $\bar{M}_i$ and $\bar{J}_i$, respectively.

Maxwell's equations (in mks units) in the frequency domain ($e^{i\omega t}$ time dependence) can be written:

$$-\nabla \times \bar{E} = i\omega\mu \bar{H} + \bar{M}_i \tag{1}$$

$$\nabla \times \bar{H} = (\sigma + i\omega\epsilon)\bar{E} + \bar{J}_i \; . \tag{2}$$

For the purposes of this report, we assume that the magnetic permeability in the earth is that of free space and neglect displacement currents in the earth. The source current is far removed so that it generates an incident plane wave at the earth's surface.

We define homogeneous-earth (incident) fields described in the earth by

$$-\nabla \times \bar{E}_i = i\omega\mu_0 \bar{H}_i + \bar{M}_i \tag{3}$$

$$\nabla \times \bar{H}_i = \sigma_1 \bar{E}_i + \bar{J}_i \; . \tag{4}$$

Subtracting (3) from (1) and (4) from (2) yields

$$\nabla \times (\bar{E} - \bar{E}_i) = -i\omega\mu(\bar{H} - \bar{H}_i) \tag{5}$$

$$\nabla \times (\bar{H} - \bar{H}_i) = \sigma \bar{E} - \sigma_1 \bar{E}_i \; . \tag{6}$$

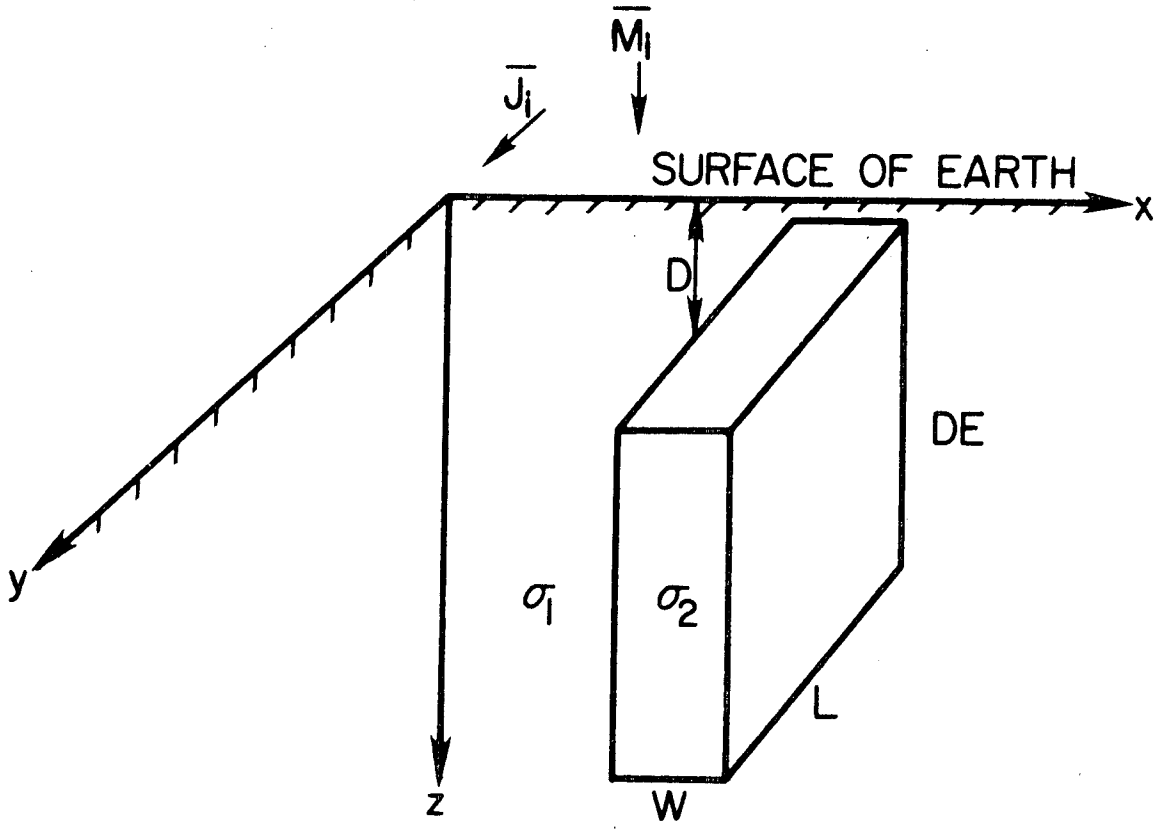

Figure 1. The three-dimensional model.

Note that σ is the actual value of conductivity: it is equal to σ_2 in the inhomogeneity and σ_1 elsewhere in the earth.

We now rewrite (6) as:

$$\nabla \times (\bar{H} - \bar{H}_i) = \sigma_1 (\bar{E} - \bar{E}_i) + (\sigma - \sigma_1) \bar{E} \quad . \qquad (7)$$

If the difference (secondary) fields are denoted by subscript "s", (5) and (7) become:

$$\nabla \times \bar{E}_s = -i\omega\mu_0 \bar{H}_s \quad , \qquad (8)$$

and

$$\nabla \times \bar{H}_s = \sigma_1 \bar{E}_s + \bar{J}_s \quad , \qquad (9)$$

where

$$\bar{J}_s = (\sigma_2 - \sigma_1) \bar{E} = \Delta\sigma \bar{E} \qquad (10)$$

is the polarization or scattering current, which exists only in the inhomogeneity.

Hence the electromagnetic field has been split into two components, denoted as incident and scattered fields. The incident, or primary, field is the field that would be present if the earth were homogeneous. It is obtained by solving (3) and (4): for the MT problem it is the field of a vertically propagating plane wave impinging on the surface of the earth.

The secondary field is due to the polarization current $\bar{J}_s$ in the inhomogeneity. It can be found by treating $\bar{J}_s$ as a source current,

converting (8) and (9) to an integral equation, and solving numerically. The secondary electric field is given by

$$\bar{E}_s = -i\omega\mu_0 \bar{A} - \nabla\varphi \,, \tag{11}$$

where $\bar{A}$ and φ are vector and scalar potentials (Harrington, 1968), given in the earth by

$$\bar{A}(\bar{r}) = \int_v \bar{J}_s(\bar{r}')\, G(\bar{r}, \bar{r}')\, dv \,, \tag{12}$$

and

$$\varphi(\bar{r}) = -\frac{1}{\sigma_1} \int_v \nabla \cdot \bar{J}_s(\bar{r}')\, G(\bar{r}, \bar{r}')\, dv \,, \tag{13}$$

where G is a scalar Green's function, which for a whole space is given by

$$G(\bar{r}, \bar{r}') = \frac{e^{-ik_1|\bar{r}-\bar{r}'|}}{4\pi|\bar{r}-\bar{r}'|} \tag{14}$$

For a body in a half space, an additional term must be added to (14) to account for image currents in the air. The additional term is different for (12) and (13). The secondary field is due to currents and charges, as defined by (11), (12), and (13). The charges occur at discontinuities in $\bar{J}_s = \Delta\sigma E$.

Adding the incident and secondary fields, we obtain an integral equation for $\bar{J}_s$:

$$\frac{1}{\Delta\sigma}\bar{J}_s = \bar{E}_i - i\omega\mu\bar{A} - \nabla\varphi \,, \tag{15}$$

which can be written symbolically as

$$\frac{1}{\Delta\sigma}\bar{J}_s(\bar{r}) = \bar{E}_i(\bar{r}) + \int \bar{\bar{G}}(\bar{r}, \bar{r}') \cdot \bar{J}_s(\bar{r}')\, dv \,, \tag{16}$$

where $\bar{\bar{G}}$ is the half-space dyadic Green's function (Tai, 1971) which accounts for the earth-air interface.

For a numerical solution, Hohmann (1975), Weidelt (1975), and Meyer

(1976) divided the body into N cubic cells as shown in Figure 2, and used pulse subsectional basis functions to represent the unknown polarization current in the body. This amounts to assuming that the current is constant throughout each cell. The integration over the dyadic Green's function can be carried out numerically (Meyer, 1976) or analytically over the volumes and surfaces of the cells (Hohmann, 1975) to obtain the equation

$$\frac{1}{\Delta\sigma}\,\bar{J}_s(\bar{r}) = \bar{E}_i(\bar{r}) + \sum_{n=1}^{N} \bar{\bar{\Gamma}}(\bar{r}, \bar{r}') \cdot \bar{J}_s^{\,n} \,, \qquad (17)$$

where $\bar{J}_s^{\,n}$ is the polarization current in cell n, and $\bar{\bar{\Gamma}}$ is the dyadic Green's function for a finite cube of current, unlike $\bar{\bar{G}}$, which applies to an infinitesimal current element. Care must be taken in deriving $\bar{\bar{\Gamma}}$, because $\bar{\bar{G}}$ is singular at $\bar{r} = \bar{r}'$.

We have derived (17) in a manner similar to that described by Hohmann (1975), except that, following Harrington (1968), we approximate the derivatives of the scalar potential in (11) with differences. Also instead of concentrating the charge (the $\nabla\cdot\bar{J}_s$ term in (13)) at the boundaries between cells, we distribute it uniformly over a volume extending from the center of one cell to the center of the next cell.

As various authors have indicated, approximating derivatives with differences provides accuracy similar to that of smooth basis functions but is much easier to implement on a computer. See, e.g., Miller and Deadrick (1974), and Butler and Wilton (1975).

Figure 3 illustrates the calculation of the x component of secondary electric field at the center of cell m due to the x component of current in

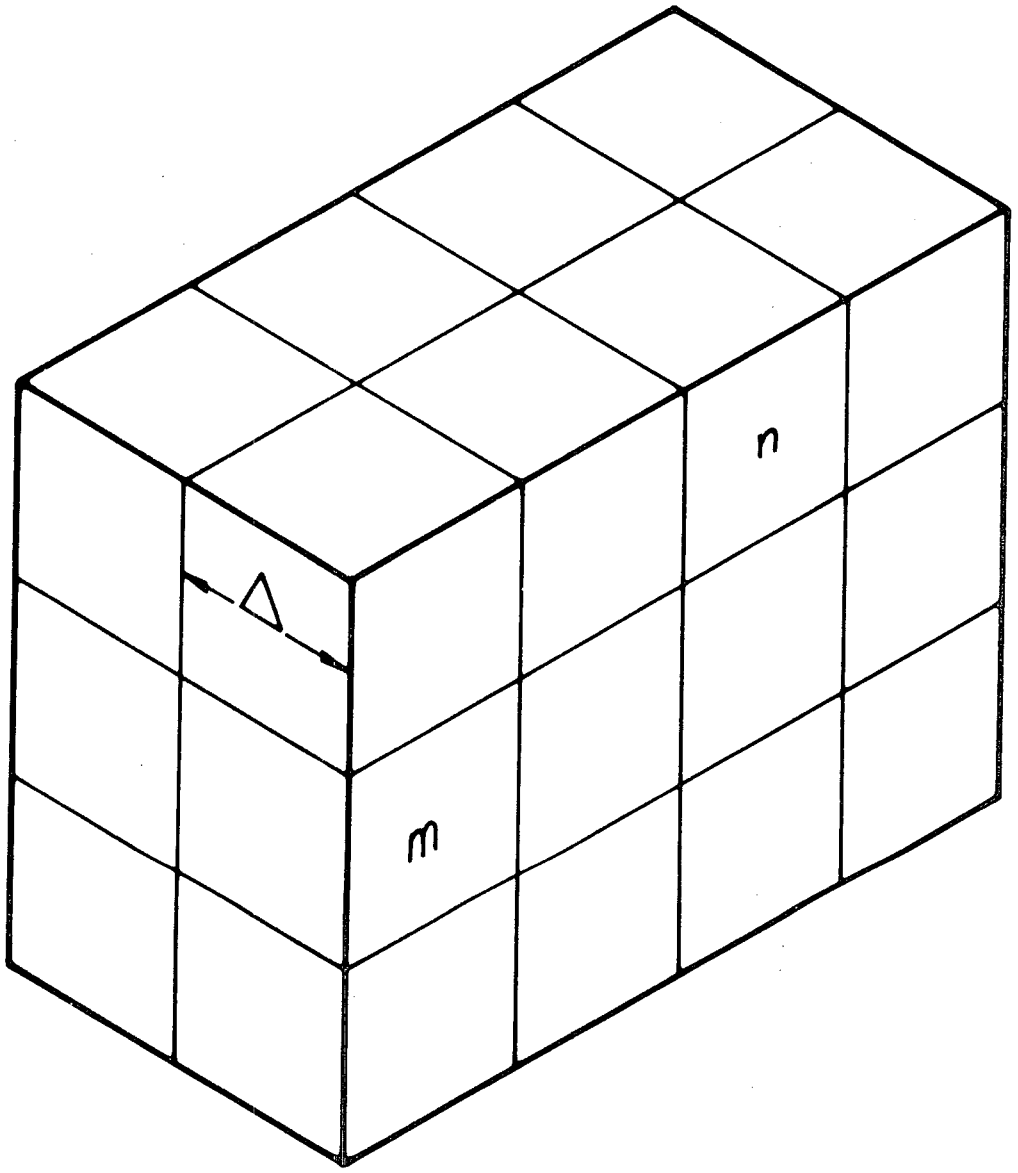

Figure 2. Body divided into cubic cells.

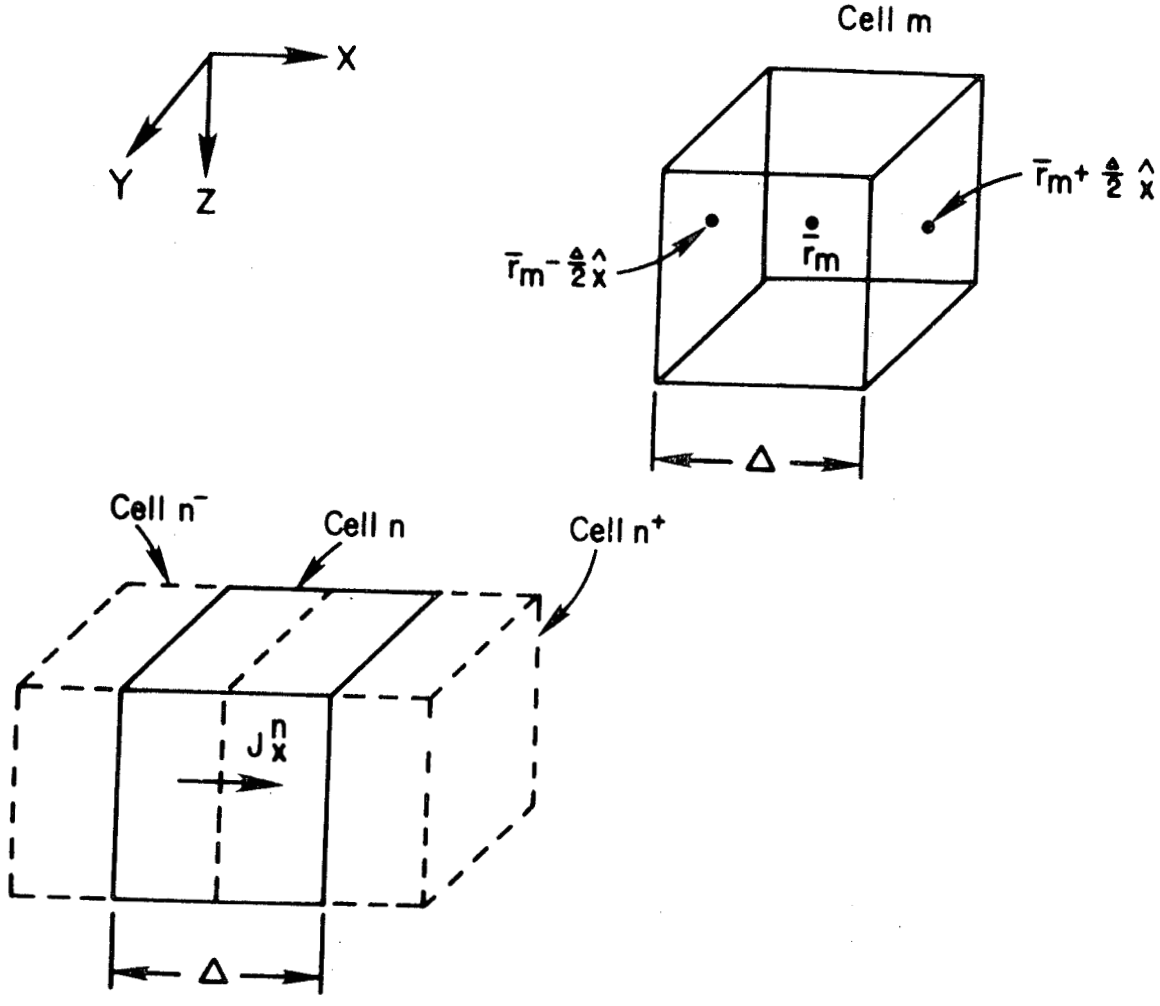

Figure 3. Illustration of geometry for calculating the matrix element Γ_{xx}^{mn}.

cell n. If we denote the center of cell m as $\bar{r}_m$, (12) becomes

$$A_x^{mn} = A_x(\bar{r}_m) = J_x^n \int_n G(\bar{r}_m, \bar{r}')\, dv, \qquad (18)$$

which is the volume current contribution.

The charge contribution to the electric field is derived from the scalar potential in (13). The derivative at the current discontinuity between cell n and cell n+1 is approximated by

$$\frac{\partial J_x}{\partial x} \approx \frac{J_x^{n+1} - J_x^n}{\Delta}, \qquad (19)$$

and is distributed uniformly in a cubic cell, denoted n^+ in Fig. 3, extending from the center of cell n to the center of cell n+1. The charge at the other end of cell n is similarly distributed over cell n^-. Then the potentials φ_{x+}^{mn} and φ_{x-}^{mn} at points $r_m + \frac{\Delta}{2}x$ and $r_m - \frac{\Delta}{2}x$ due to J_x^n are given by (13), which becomes

$$\varphi_{x+}^{mn} = \frac{J_x^n}{\sigma_1 \Delta}\left[-\int_{n^-} G(\bar{r}_m + \tfrac{\Delta}{2}\hat{x}, \bar{r}')dv + \int_{n^+} G(\bar{r}_m + \tfrac{\Delta}{2}\hat{x}, \bar{r}')\, dv\right] \qquad (20)$$

and

$$\varphi_{x-}^{mn} = \frac{J_x^n}{\sigma_1 \Delta}\left[-\int_{n^-} G(\bar{r}_m - \tfrac{\Delta}{2}\hat{x}, \bar{r}')\, dv + \int_{n^+} G(\bar{r}_m - \tfrac{\Delta}{2}\hat{x}, \bar{r}')\, dv\right]. \qquad (21)$$

Finally, E_x is given by (11), which becomes

$$E_{xs}^{mn} = -i\omega\mu_0 A_x^{mn} - \left(\varphi_{x+}^{mn} - \varphi_{x-}^{mn}\right). \qquad (22)$$

In terms of the method of moments, this solution is equivalent to using pulse functions for both current and charge and approximating the operator. To obtain $\bar{\bar{\Gamma}}$ in (17), we need to evaluate the integrals in (18), (20), and

(21) for each cartesian component of current. The integrals all are of the same form: the scalar Green's function integrated over a cubic cell.

We can write $\overline{\overline{\Gamma}}$ as the sum of two components representing current and charge sources:

$$\overline{\overline{\Gamma}} = \overline{\overline{\Gamma}}_A + \overline{\overline{\Gamma}}_\phi , \tag{23}$$

where, for illustration, the x component of secondary electric field at the center of cell m due to the x component of polarization current in cell n is given by

$$E_{xs}^{mn} = \left[\Gamma_{A}^{mn}_{xx} + \Gamma_{\phi}^{mn}_{xx} \right] J_x^n \tag{24}$$

From (18) and (22),

$$\Gamma_{A}^{mn}_{xx} = -i\omega\mu_0 \int_n G(\bar{r}_m, \bar{r}')\, dv , \tag{25}$$

while from (20), (21), and (22),

$$\Gamma_{\phi}^{mn}_{xx} = -\frac{1}{\sigma_1 \Delta} \left[-\int_{n^-} G(\bar{r}_m + \tfrac{\Delta}{2}\hat{x}, \bar{r}')dv + \int_{n^+} G(\bar{r}_m + \tfrac{\Delta}{2}\hat{x}, \bar{r}')dv \right.$$

$$\left. -\int_{n^-} G(\bar{r}_m - \tfrac{\Delta}{2}\hat{x}, \bar{r}')dv + \int_{n^+} G(\bar{r}_m - \tfrac{\Delta}{2}\hat{x}, \bar{r}')dv \right] . \tag{26}$$

The other elements of the dyadic Green's function can be derived by analogy. For our half-space problem, another term, which is given by Hohmann (1975) must be added to G.

Because the electric field due to the volume current is in the same

direction as the current, the off-diagonal elements of the dyadic Green's function contain only the charge term. Thus, for example the y component of secondary electric field at the center of cell m due to the x component of polarization current in cell n is given by

$$E_{ys}^{mn} = \Gamma_{\Phi}^{mn}{}_{yx} \cdot J_x^n \quad . \tag{27}$$

In more concise notation, (17) becomes

$$\frac{\bar{J}_s^m}{\Delta\sigma} = \bar{E}_i^m + \sum_{n=1}^{N} \bar{\bar{\Gamma}}_{mn} \cdot \bar{J}_s^n \quad , \tag{28}$$

where $\bar{J}_s^m$ and $\bar{J}_s^n$ are the polarization currents in cells m and n, respectively. Rearranging (28) yields

$$\sum_{n=1}^{N} \left[\bar{\bar{\Gamma}}_{mn} - \frac{1}{\Delta\sigma} \bar{\bar{\delta}}_{mn} \right] \cdot \bar{J}_s^n = - \bar{E}_i^m \quad , \tag{29}$$

in which

$$\bar{\bar{\delta}}_{mn} = \begin{cases} \bar{\bar{I}} \quad , & m = n \\ \bar{\bar{0}} \quad , & m \neq n \end{cases} \quad ,$$

where $\bar{\bar{I}}$ is the unit dyadic and $\bar{\bar{0}}$ is the null dyadic.

Writing (29) for each for the N values of m yields a partitioned matrix equation

$$\left[\bar{\bar{Z}} \right] \cdot \left[\bar{J}_s \right] = - \left[\bar{E}_i \right] \tag{30}$$

to solve for the polarization current in the body. The elements of the impedance matrix are themselves 3x3 matrices, given by

$$\bar{\bar{Z}}_{mn} = \bar{\bar{\Gamma}}_{mn} - \frac{1}{\Delta\sigma}\,\bar{\bar{\delta}}_{mn} \qquad (31)$$

Note that (30) also can be written as

$$\left[\bar{\bar{Z}}_1 + \bar{\bar{Z}}_2\right] \cdot \left[\bar{J}_s\right] = -\left[\bar{E}_i\right], \qquad (32)$$

where $\bar{\bar{Z}}_1$ describes the geometry, frequency, and background conductivity, while $\bar{\bar{Z}}_2$ is a diagonal matrix which depends on the conductivity of the body.

In Cartesian coordinates, (30) becomes

$$\sum_{n=1}^{N}\left[\left(\Gamma_{xx}^{mn} - \frac{\delta_{mn}}{\Delta\sigma}\right)J_x^n + \Gamma_{xy}^{mn}J_y^n + \Gamma_{xz}^{mn}J_z^n\right] = -E_{ix}^m \qquad (33)$$

$$\sum_{n=1}^{N}\left[\Gamma_{yx}^{mn}J_x^n + \left(\Gamma_{yy}^{mn} - \frac{\delta_{mn}}{\Delta\sigma}\right)J_y^n + \Gamma_{yz}^{mn}J_z^n\right] = -E_{iy}^m \qquad (34)$$

$$\sum_{n=1}^{N}\left[\Gamma_{zx}^{mn}J_x^n + \Gamma_{zy}^{mn}J_y^n + \left(\Gamma_{zz}^{mn} - \frac{\delta_{mn}}{\Delta\sigma}\right)J_z^n\right] = -E_{iz}^m \qquad (35)$$

The matrix is formed by arranging the equations as follows:

$$\left(\Gamma_{xx}^{11} - \frac{1}{\Delta\sigma}\right)J_x^1 + \Gamma_{xy}^{11}J_y^1 + \Gamma_{xz}^{11}J_z^1 + \cdots + \Gamma_{xx}^{1N}J_x^N + \Gamma_{xy}^{1N}J_y^N + \Gamma_{xz}^{1N}J_z^N = -E_{xi}^1$$

$$\Gamma_{yx}^{11}J_x^1 + \left(\Gamma_{yy}^{11} - \frac{1}{\Delta\sigma}\right)J_y^1 + \Gamma_{yz}^{11}J_z^1 + \cdots + \Gamma_{yx}^{1N}J_x^N + \Gamma_{yy}^{1N}J_y^N + \Gamma_{yz}^{1N}J_z^N = -E_{yi}^1$$

$$\Gamma_{zx}^{11}J_x^1 + \Gamma_{zy}^{11}J_y^1 + \left(\Gamma_{zz}^{11} - \frac{1}{\Delta\sigma}\right)J_z^1 + \cdots + \Gamma_{zx}^{1N}J_x^N + \Gamma_{zy}^{1N}J_y^N + \Gamma_{zz}^{1N}J_z^N = -E_{zi}^1$$

$$\Gamma^{21}_{xx} J^1_x + \Gamma^{21}_{xy} J^1_y + \Gamma^{21}_{xz} J^1_z + \left(\Gamma^{22}_{xx} - \frac{1}{\Delta\sigma}\right) J^2_x + \cdots$$

$$+ \Gamma^{2N}_{xy} J^N_y + \Gamma^{2N}_{xz} J^N_z = -E^2_{xi}$$

$$\vdots$$

$$\Gamma^{N1}_{zx} J^1_x + \Gamma^{N1}_{zy} J^1_y + \Gamma^{N1}_{zz} J^1_z + \cdots + \Gamma^{NN}_{zy} J^N_y$$

$$+ \left(\Gamma^{NN}_{zz} - \frac{1}{\Delta\sigma}\right) J^N_z = -E^N_{zi} \,.$$

The next step is to compute the elements of the dyadic Green's function for a cube of current:

$$\Gamma^{mn}_{uv} = \Gamma^{mn}_{uv\,A} + \Gamma^{mn}_{uv\,\varphi} \,, \tag{37}$$

where uv stands for permutations of the cartesian coordinates x, y, z. We divide $\bar{\bar{\Gamma}}_A$ and $\bar{\bar{\Gamma}}_\varphi$ into primary and secondary parts, where the secondary parts account for the earth-air interface, as described by Hohmann (1975). Thus

$$\Gamma^{mn}_{uv\,A} = \Gamma^{mn}_{uv\,AP} + \Gamma^{mn}_{uv\,AS} \,, \tag{38}$$

and

$$\Gamma^{mn}_{uv\,\varphi} = \Gamma^{mn}_{uv\,\varphi P} + \Gamma^{mn}_{uv\,\varphi S} \,. \tag{39}$$

With the exception of $\Gamma^{mn}_{uv\,\varphi P}$, which is illustrated in (26), the dyadic Green's function elements are as described by Hohmann (1975). The integrals in (25) and (26) only need to be evaluated for the primary parts of the Green's function, and they all have the same form:

$$I = \int_V \frac{e^{-ik_1|\bar{r}_0 - \bar{r}'|}}{4\pi|\bar{r}_0 - \bar{r}'|}\, dv \,. \tag{40}$$

The shape of the cell is not important for this volume integration, so we replace the cube by a sphere of the same volume and integrate analytically as described by Hohmann (1975). When the field point, $\bar{r}_0$, is at the center of the sphere we can integrate through the singularity to obtain

$$I = \frac{1}{k_1^2}\left[(ik_1a + 1)e^{-ik_1a} - 1\right], \tag{41}$$

where a is the radius of the sphere.

When $\bar{r}_0$ is outside the sphere, we have

$$I = \frac{e^{-ik_1R}}{k_1^3 R}\left[\sin(k_1a) - k_1a\cos(k_1a)\right], \tag{42}$$

where

$$R = |\bar{r}_0 - \bar{r}_c|$$

with $\bar{r}_c$ the center of the sphere.

MAGNETOTELLURIC SPECIALIZATION

The MT source field is a vertically propagating plane wave impinging on the surface of the earth. If the electric field of the incident wave is in the y direction, and if we denote its amplitude by E_0, then the total electric field at the surface of the earth in the absence of the inhomogeneity is (Hohmann, 1971)

$$E_y^i = E_0 \frac{2k_0}{k_0 + k_1} \approx 2 E_0 \frac{k_0}{k_1} , \tag{43}$$

with

$$k_0 = (\omega^2 \mu_0 \varepsilon_0)^{1/2}$$

$$k_1 = (-i\omega\mu_0\sigma_1)^{1/2}$$

for the low frequencies of interest here.

In the earth we have

$$E_y^i = 2 E_0 \frac{k_0}{k_1} e^{-ik_1 z} , \tag{44}$$

which is the incident, or primary, field for our integral equation solution.

The primary magnetic field at the earth's surface is

$$H_x^i = -2 E_0 \frac{k_0}{\omega\mu_0} = -2 E_0 \left(\frac{\varepsilon_0}{\mu_0}\right)^{1/2} \tag{45}$$

For the simple model which we consider in this report (Fig. 1), there are two vertical planes of symmetry passing through the center of the body. Hence it is only necessary to solve for one-fourth of the total number of unknowns.

Consider the 96-cube model numbered as shown in Fig. 4. The incident electric field is oriented in the x direction. It is easy to see that the

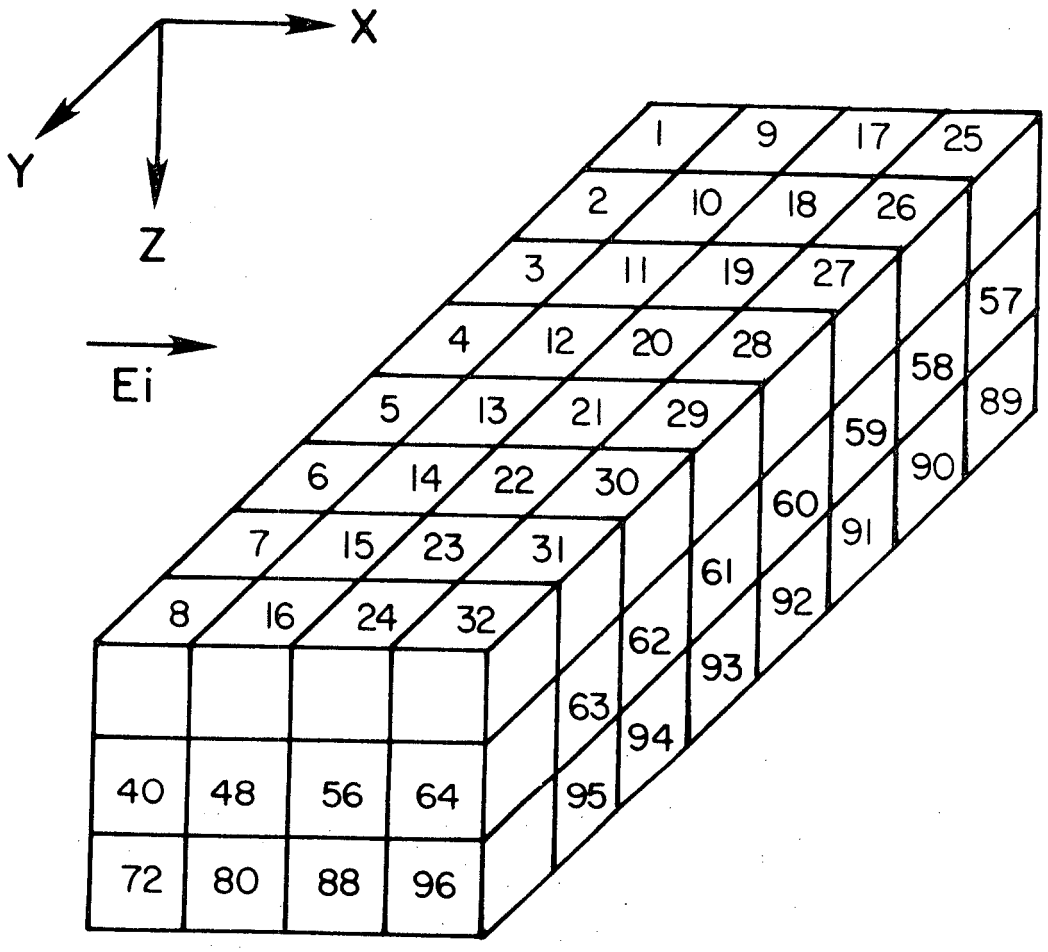

Figure 4. MT model with two symmetry planes.

polarization currents in the various cells are interelated as follows:

$$J_x^1 = J_x^8 = J_x^{25} = J_x^{32}$$

$$J_y^1 = -J_y^8 = -J_y^{25} = J_y^{32}$$

$$J_z^1 = J_z^8 = -J_z^{25} = -J_z^{32}$$

$$J_x^2 = J_x^7 = J_x^{26} = J_x^{31}$$

$$\vdots$$

$$J_z^4 = J_z^5 = -J_z^{28} = -J_z^{29}$$

$$J_x^9 = J_x^{16} = J_x^{17} = J_x^{24}$$

$$\vdots$$

$$J_z^{12} = J_z^{13} = -J_z^{20} = -J_z^{21}$$

$$J_x^{33} = J_x^{40} = J_x^{57} = J_x^{64}$$

$$\vdots$$

$$J_z^{76} = J_z^{77} = -J_z^{84} = -J_z^{85}$$

Thus, when there are two symmetry planes, the system of equations (36) becomes:

$$\left(\Gamma^{1,1}_{xx} - \frac{1}{\Delta\sigma} + \Gamma^{1,8}_{xx} + \Gamma^{1,25}_{xx} + \Gamma^{1,32}_{xx}\right) J^1_x + \left(\Gamma^{1,1}_{xy} - \Gamma^{1,8}_{xy} - \Gamma^{1,25}_{xy} + \Gamma^{1,32}_{xy}\right) J^1_y$$

$$+ \left(\Gamma^{1,1}_{xz} + \Gamma^{1,8}_{xz} - \Gamma^{1,25}_{xz} - \Gamma^{1,32}_{xz}\right) J^1_z + \cdots + (---)\, J^4_z$$

$$+ (---)\, J^9_x + \cdots + (---)\, J^{12}_z + \cdots + (---)\, J^{76}_z = -E^{1,c}_x$$

$$\left(\Gamma^{1,1}_{yx} + \Gamma^{1,8}_{yx} + \Gamma^{1,25}_{yx} + \Gamma^{1,32}_{yx}\right) J^1_x + \left(\Gamma^{1,1}_{yy} - \frac{1}{\Delta\sigma} - \Gamma^{1,8}_{yy} - \Gamma^{1,25}_{yy} + \Gamma^{1,32}_{yy}\right) J^1_y$$

$$+ \left(\Gamma^{1,1}_{yz} + \Gamma^{1,8}_{yz} - \Gamma^{1,25}_{yz} - \Gamma^{1,32}_{yz}\right) J^1_z + \cdots + (---)\, J^4_z + (---)\, J^9_x$$

$$+ \cdots + (---)\, J^{12}_z + \cdots + (---)\, J^{76}_z = -E^{1,c}_y$$

$$\vdots$$

It is necessary to solve for the unknown current only in cells 1-4, 9-12, 33-36, 41-44, 65-68, and 73-76, i.e., one-fourth of the total unknowns.

Unfortunately the new matrix, defined by equations (46), is not symmetric as in the general case (36) for equal-conductivity and equal-size cells. Even so, the computer storage and computation time are reduced considerably for the MT problem. Without symmetry planes $3N(3N+1)/2 \approx 9N^2/2$ storage locations are required, where N is the number of cells. With two symmetry planes, the

storage requirement is $\frac{3N}{4} \times \frac{3N}{4} = \frac{9N^2}{16}$ ---less by a factor of 8.

Figure 5 illustrates the reduction in computer time for a two-symmetry-plane problem compared to one with no symmetry. In each case, forming and factoring (LU decomposition) the matrix account for most of the computer time. Matrix factorization time is less by a factor of about 35 when symmetry is invoked. The time required to form the matrix is less for the symmetric problem, because only one-fourth of the matrix elements need to be computed.

In the general case a maximum of 120 cells can be used on the University of Utah Univac 1108 computer, but for the symmetric problem the limitation is 340 cells. This increase in the number of cells permits the use of smaller cells for more accuracy, or, alternatively, the modeling of larger bodies.

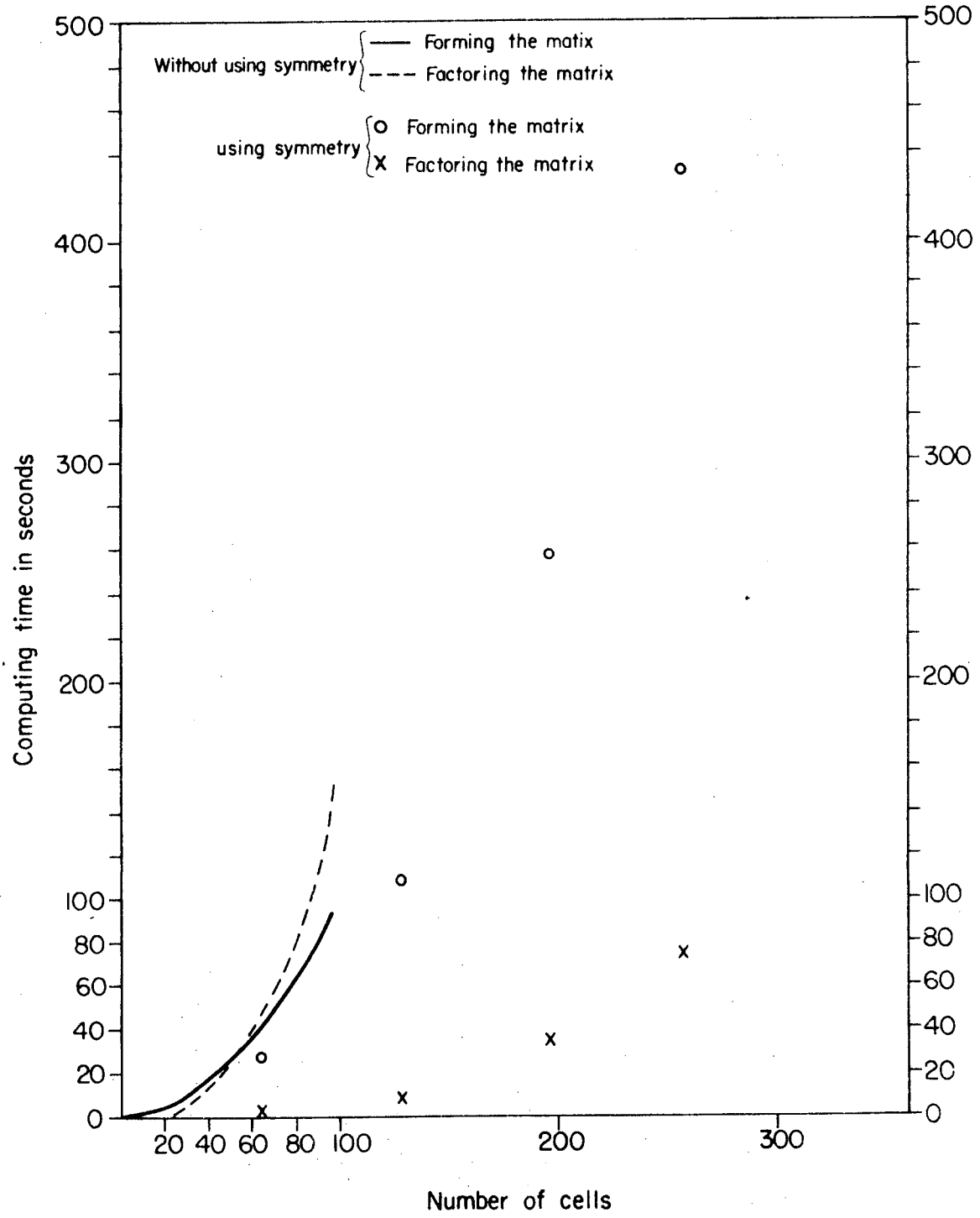

Figure 5. Reduction in computer time for problem with two symmetry planes.

CONVERGENCE CHECKS

Because of the many possibilities for theoretical and programming errors, it is important to verify the accuracy of any numerical solution. The best check is with results from another type of numerical solution. Unfortunately, the only other published 3D MT results are those of Jones (1974), Weidelt (1975), and Reddy et al., (1977), all for outcropping bodies which we cannot model accurately. However, comparisons with Pridmore (1978) for controlled-source EM, comparisons with other solutions for zero frequency (Hohmann, 1975), and comparisons with 2D models discussed later in this report lend credence to our results. Also the general behavior of the 3D MT results is as expected.

An important self-check is convergence: as the cells are made smaller, the results should converge to some value. The body that we have used to check convergence is shown in Figure 6. It is a 1 km x 2 km x 2 km conductive prism at 1 km depth and is elongated in the y direction. We have checked convergence at points A, B, and C at four frequencies and at three different discretizations: 1x2x2 = 4 cells, 2x4x4 = 32 cells, and 4x8x8 = 256 cells. The cell sizes for these three cases are 1 km, 0.5 km, and 0.25 km, respectively. The two excitation modes - E_{11} and $E_{\perp}$ - are illustrated in Fig. 6a. For E_{11} excitation the incident electric field is parallel to the long axis of the body, while for $E_{\perp}$ excitation the incident electric field is perpendicular to the long axis.

Figures 7-9 show the convergence as a function of frequency at points A, B, and C, respectively, for the E_{11} mode. Results are given in terms of

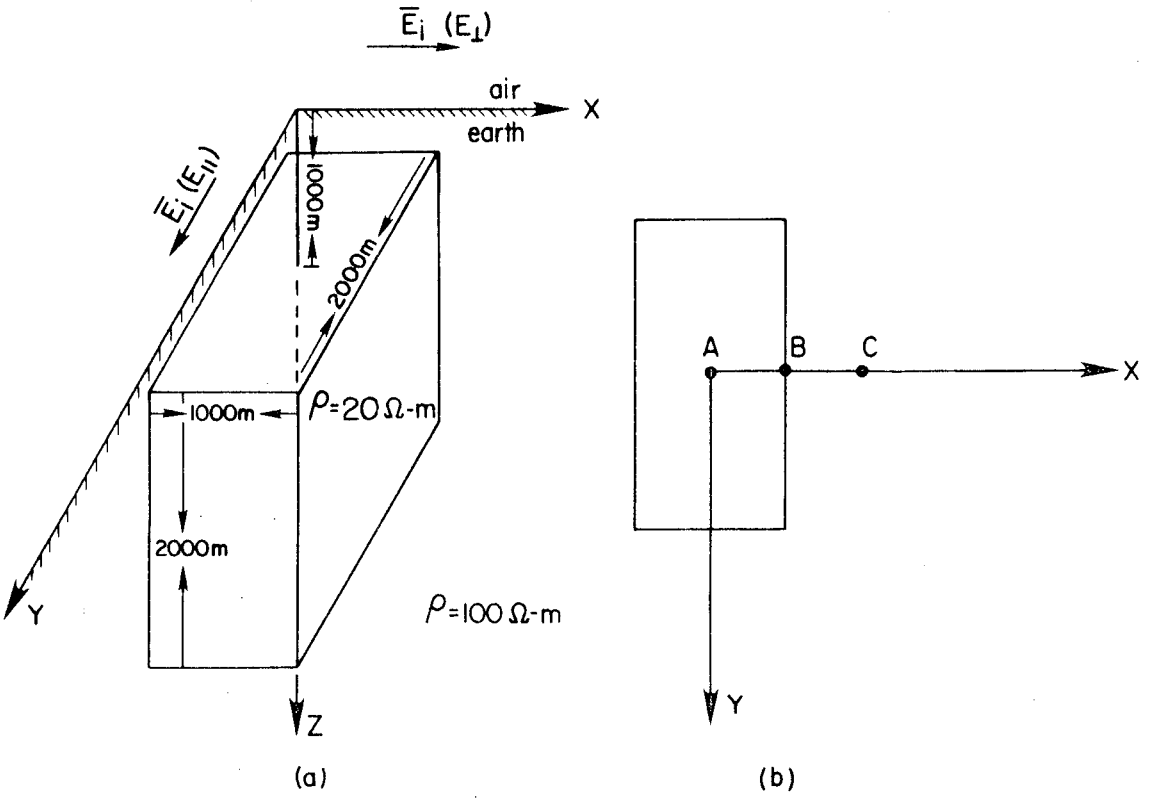

Figure 6. (a) Three dimensional model for convergence checks.
(b) Plan view showing the three observation points on the surface of the earth.

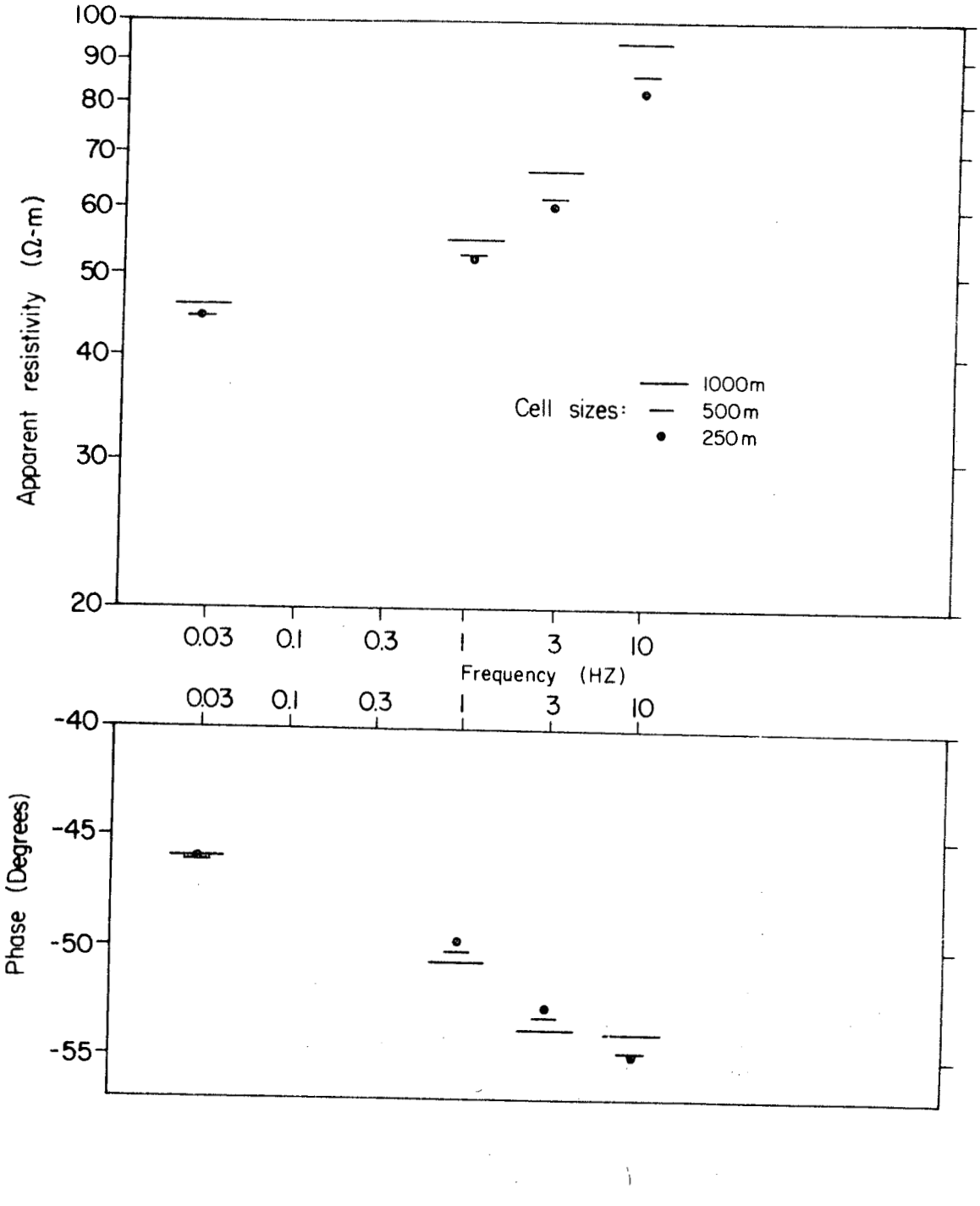

Figure 7. Convergence at point A for E_{11} excitation.

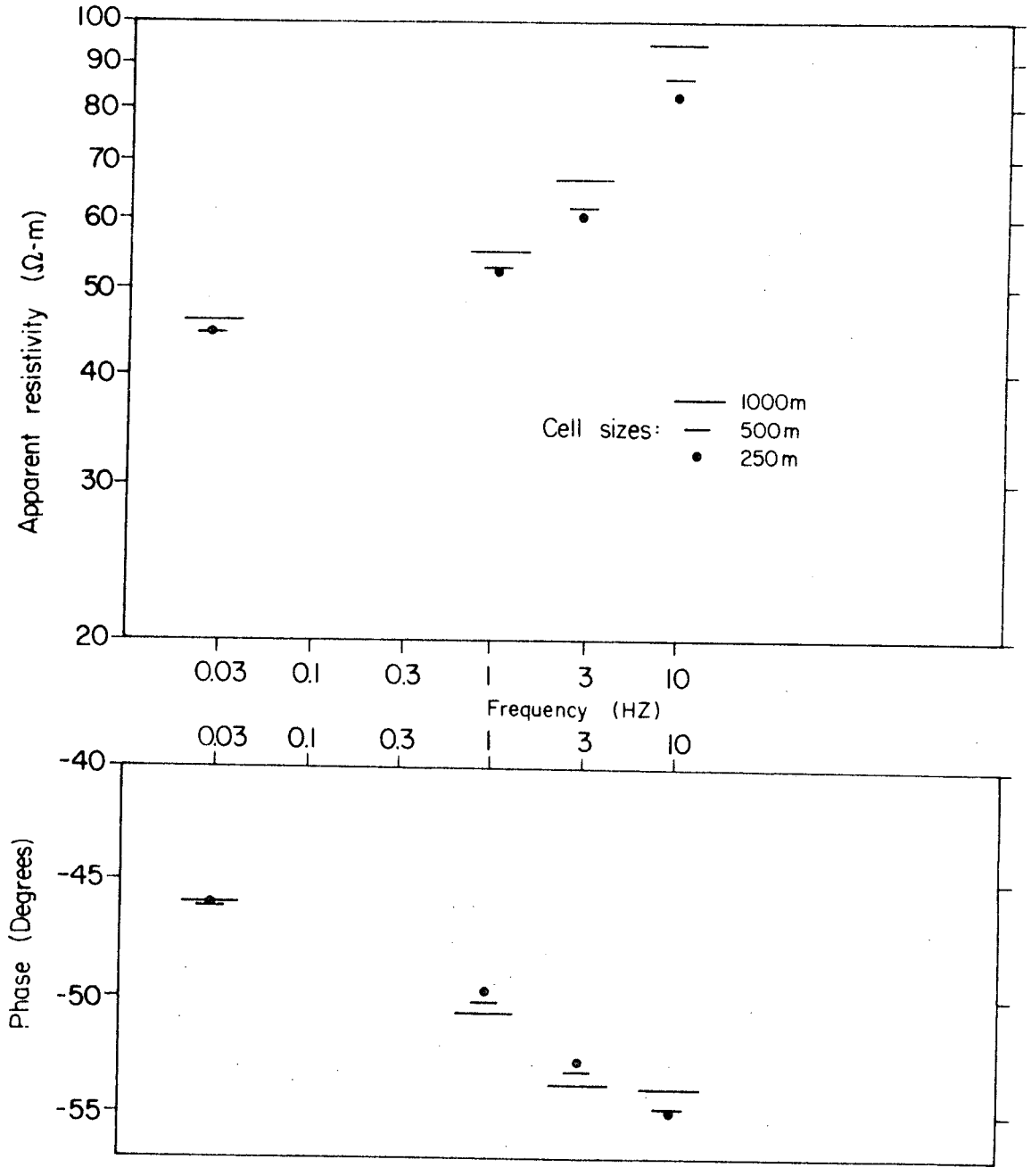

Figure 8. Convergence at point B for E_{11} excitation.

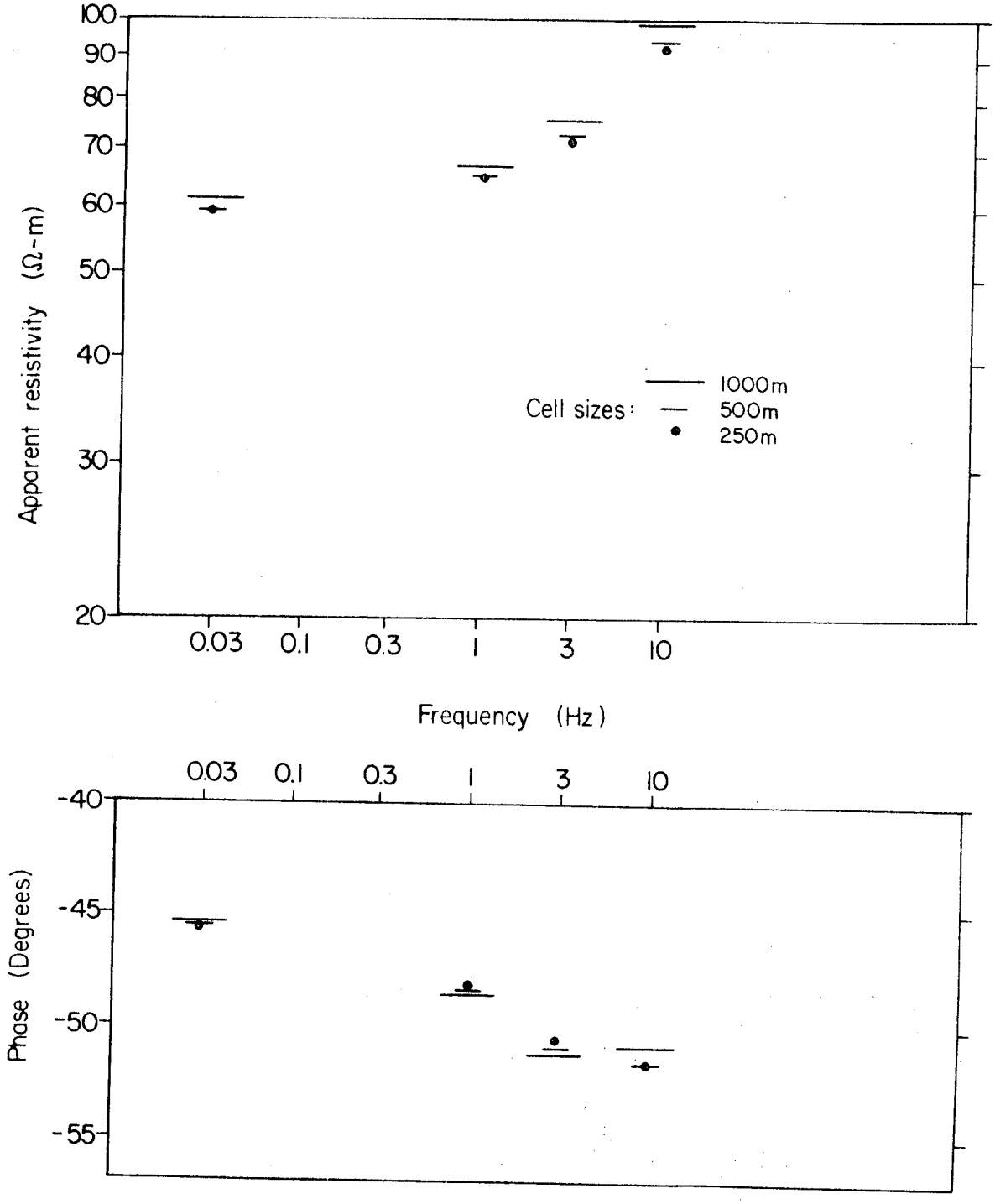

Figure 9. Convergence at point C for E_{11} excitation.

apparent resistivity (ρ_{yx}) and phase (E_y phase - H_x phase). The solution is convergent, and, as expected, smaller cells are required to represent the current at the higher frequencies.

At 10 Hz the cell sizes represented in Figures 7-9 are 2.8, 1.4, and 0.7 skin depths in the body. At 1 Hz, where the solution has converged to the final result by the middle cell size, the cell sizes are 0.89, 0.44, 0.22 skin depths in the body. Thus it appears that the minimum cell size for accurate results in this case is about 0.5 skin depths. Of course larger cells may be adequate for particular interpretation problems and computations would be less expensive. Another cell-size criterion, which depends mainly on conductivity contrast and depth, is that the cells must be small enough to accurately represent the current even at very low frequencies where the skin depth is large. As a rule of thumb, we require the cells to be no larger than the depth. As a result, computations for shallow bodies are expensive.

Convergence for $E_\perp$ excitation is a little faster, as illustrated in Figures 10-12.

The significance of these results is that we have been able to halve the cell size two times and demonstrate convergence for this particular integral equation solution. In our previous controlled-source modeling there were no symmetry planes, so that only two discretization levels were possible, and it was impossible to determine whether the solution is convergent except in the simple zero-frequency case. Higher-order basis functions would yield the same accuracy with fewer unknowns, but they would be difficult to implement.

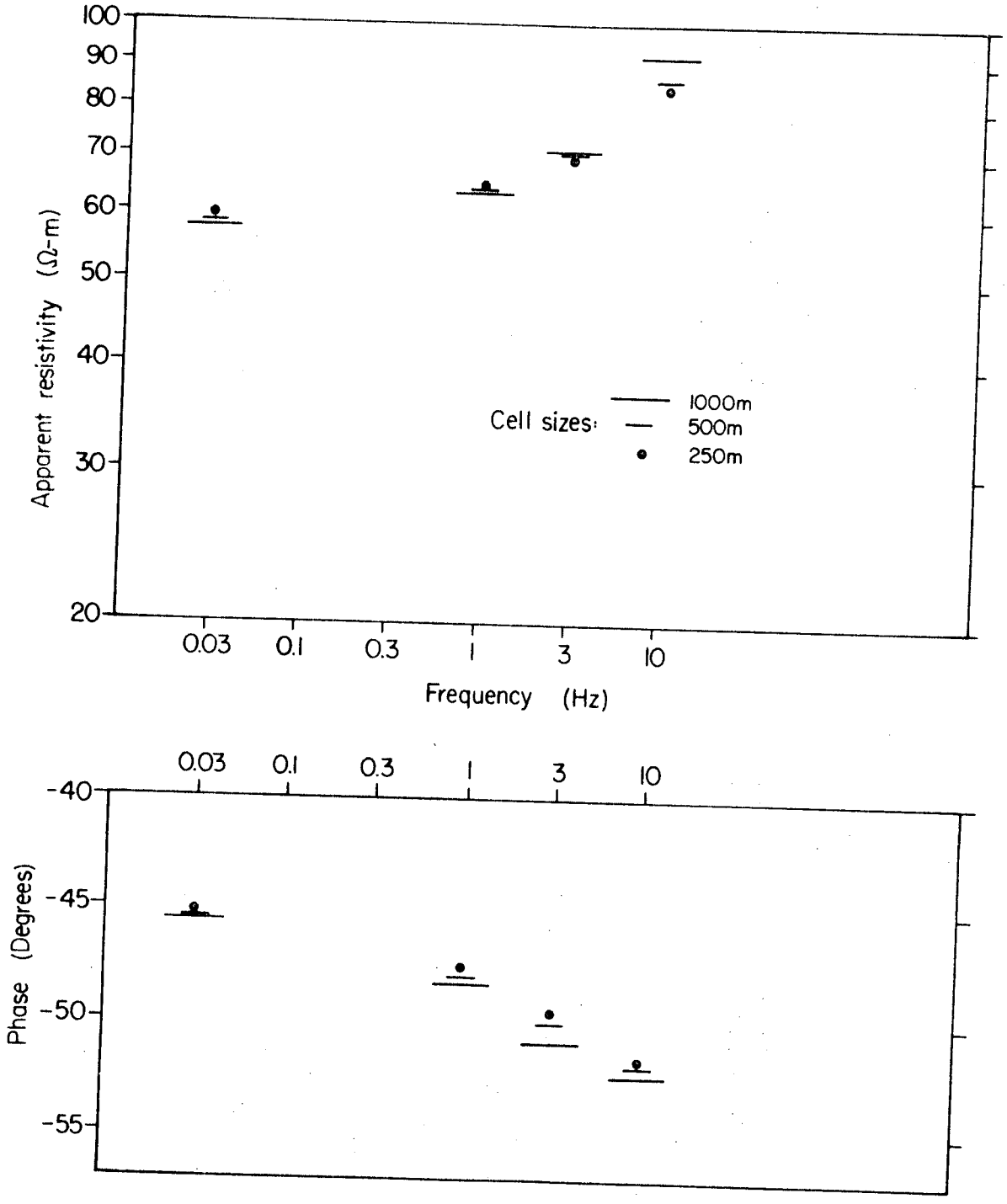

Figure 10. Convergence at point A for $E_{\perp}$ excitation.

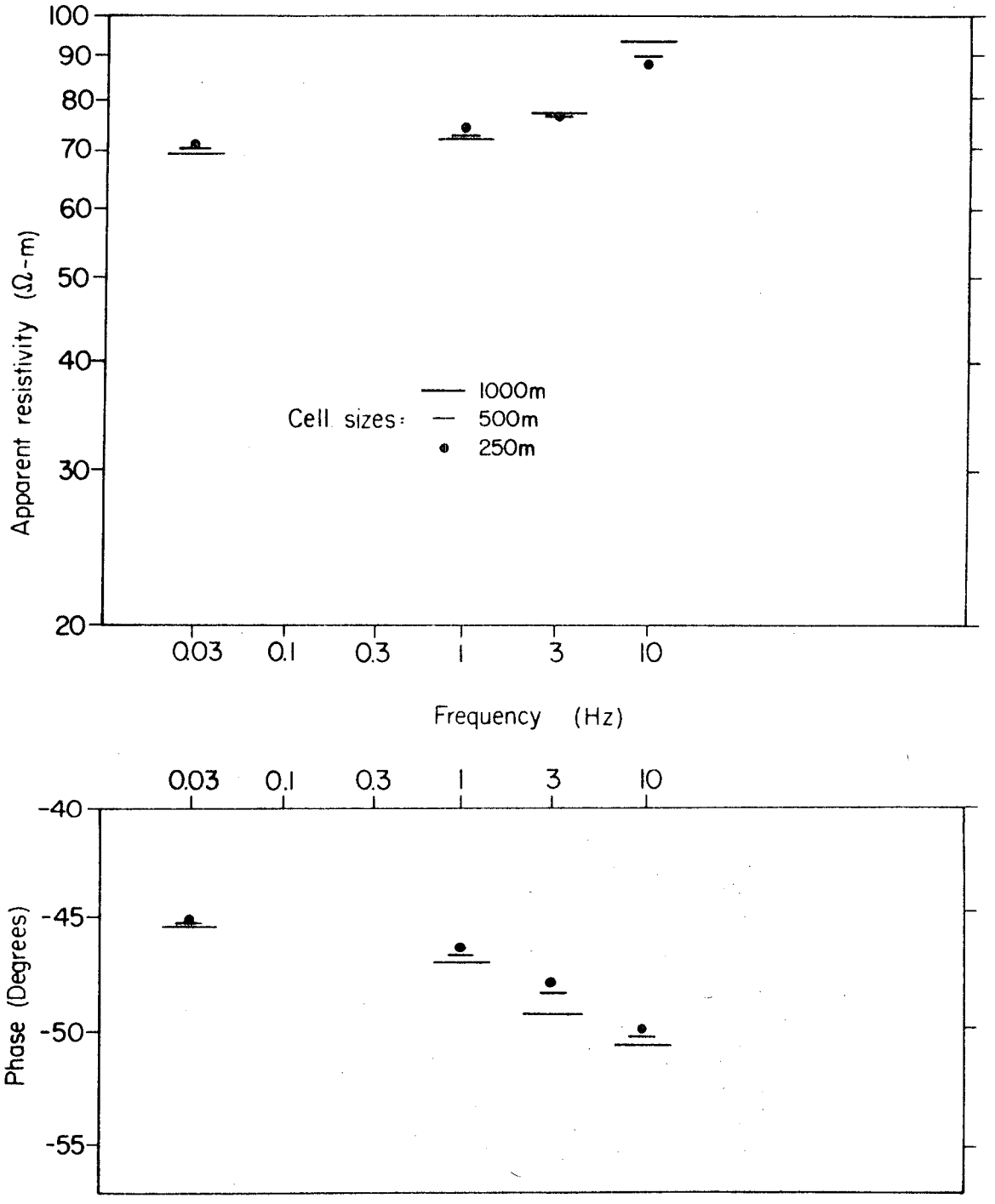

Figure 11. Convergence at point B for $E_{\perp}$ excitation.

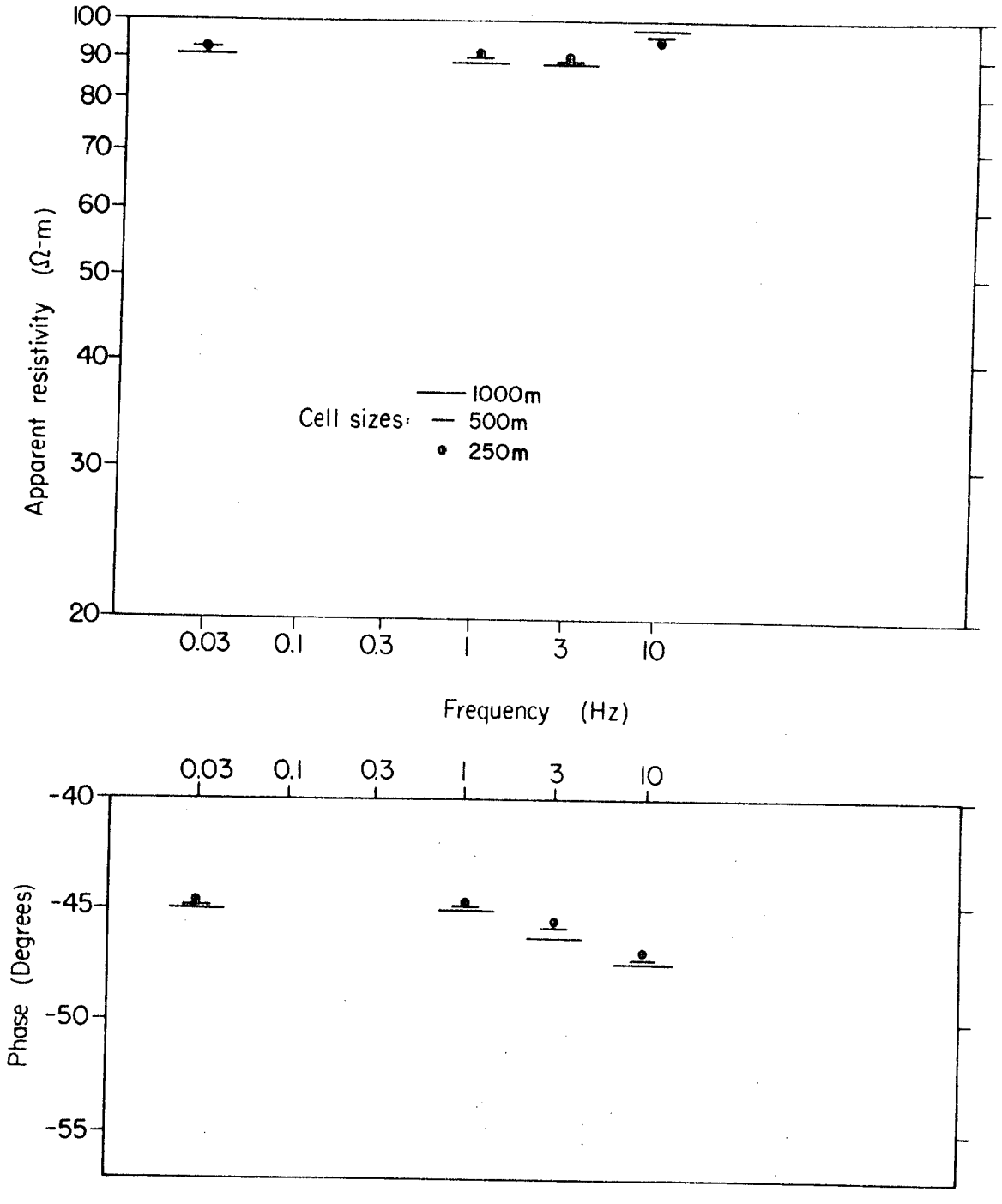

Figure 12. Convergence at point C for $E_{\perp}$ excitation.

COMPARISON WITH 2D MODELS

Another useful check, and one which is enlightening for MT interpretation, is comparison with 2D models. As the length of the 3D body increases, the fields should approach those of a 2D model. Figures 13 and 14 show comparisons between our 3D results and 2D results computed with Rijo's (1977) finite element algorithm. The model is that of Figure 6 with variable strike length (2, 4, 8, ∞ km).

Figure 13 shows the comparison for E_{11} excitation which corresponds to the 2D TE mode. Only E_y, H_x, and H_z components are present for the 2D model, but all five components - E_x, E_y, H_y, H_z - are present in the 3D case. Apparent resistivity (ρ_{yx}) and phase (E_y phase - H_x phase) are plotted against distance from the center of the body for the three strike lengths and for the 2D body.

Because there are no boundaries normal to current flow to generate space charges in the 2D TE case, whereas there are in the 3D model, the results are quite different. The difference is particularly great at 0.03 Hz. The secondary electric field due to polarization charge at the ends of the body is present even at zero frequency while that due to volume polarization current (the only source of secondary field in the 2D case) decreases with decreasing frequency. The secondary magnetic field, which is due only to volume polarization current, also has a frequency-independent component.

At 1 Hz and above, apparent resistivities for the 8 km-long 3D body are very close to those of the 2D model. Phase seems to converge to 2D values as

the length is increased, but a body longer than 8 km would be required for good agreement.

Comparisons between our 3D $E_{\perp}$ results and Rijo's 2D TM results are shown in Figure 14. Space charges are included implicitly in the 2D TM formulation, so that the two solutions do not diverge at low frequencies as they do for E_{11} excitation. However, except at the highest frequency, the 3D solution seems to converge to values slightly different from those of the 2D solution as the length of the body increases. For example, the apparent resistivity amplitudes differ by as much as 15 percent at 1 Hz.

This discrepancy in the $E_{\perp}$ results could be due either to the 2D or 3D solution. While the accuracy of the 2D finite element TE results has been verified by cross checks with other numerical solutions (Hohmann, 1971; Swift, 1971), we noted some discrepancies in comparing the TM finite element reults with those of Swift. This discrepancy is being investigated, but the comparison in Figure 14 is adequate to give us confidence in our 3D results.

The comparisons in Figures 13 and 14 are useful for two reasons: (1) They confirm the validity of the 3D solution, and (2) they point out the problems in interpreting data with 2D models. Because there are lateral conductivity boundaries in all directions for a typical geothermal application of MT, there really is no TE mode. As deduced by Wannamaker (1978), standard mode identification is invalid, and 3D models are required for interpretation.

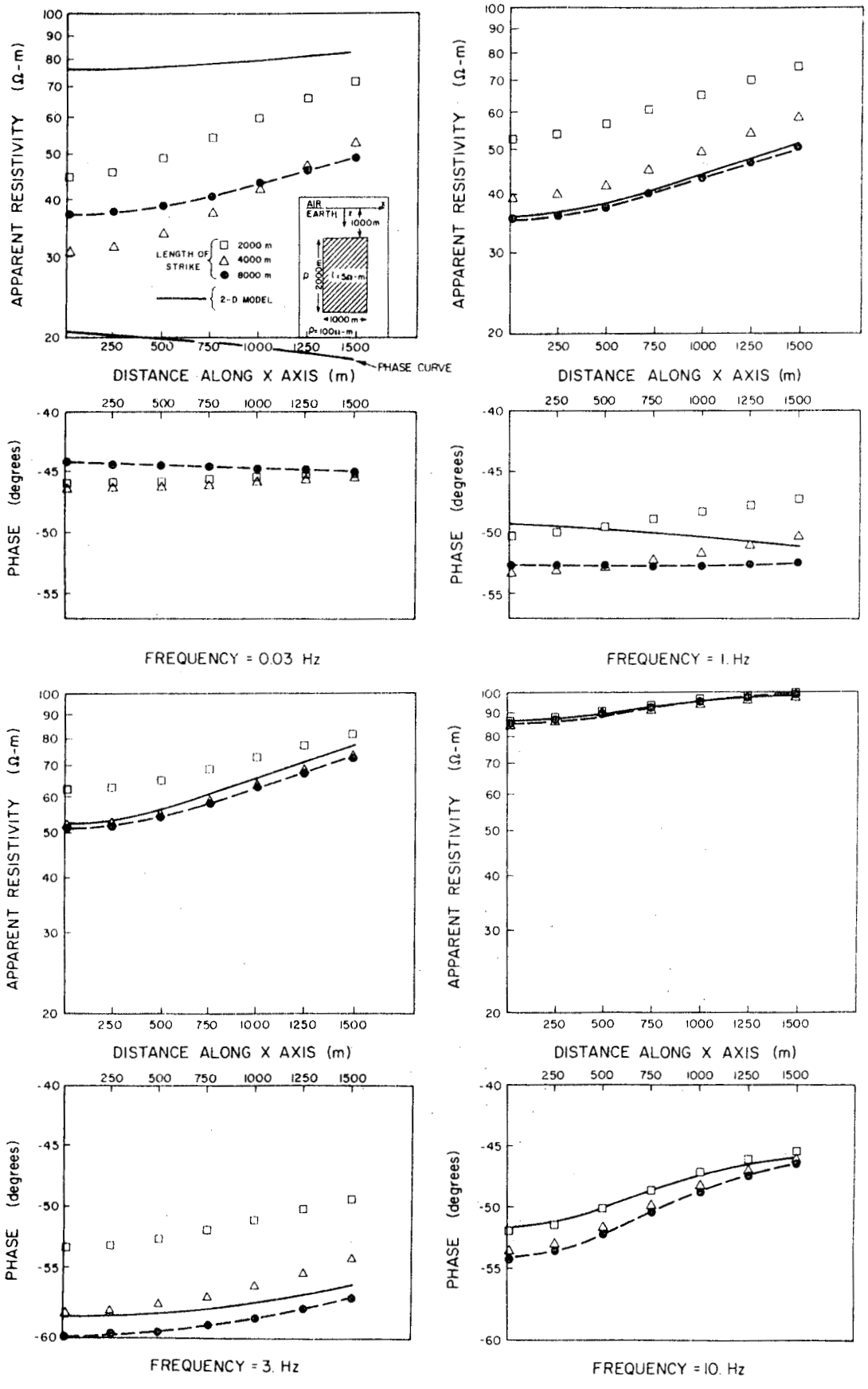

Figure 13. Comparison between 2D results and 3D results for bodies of different length - E_{11} excitation.

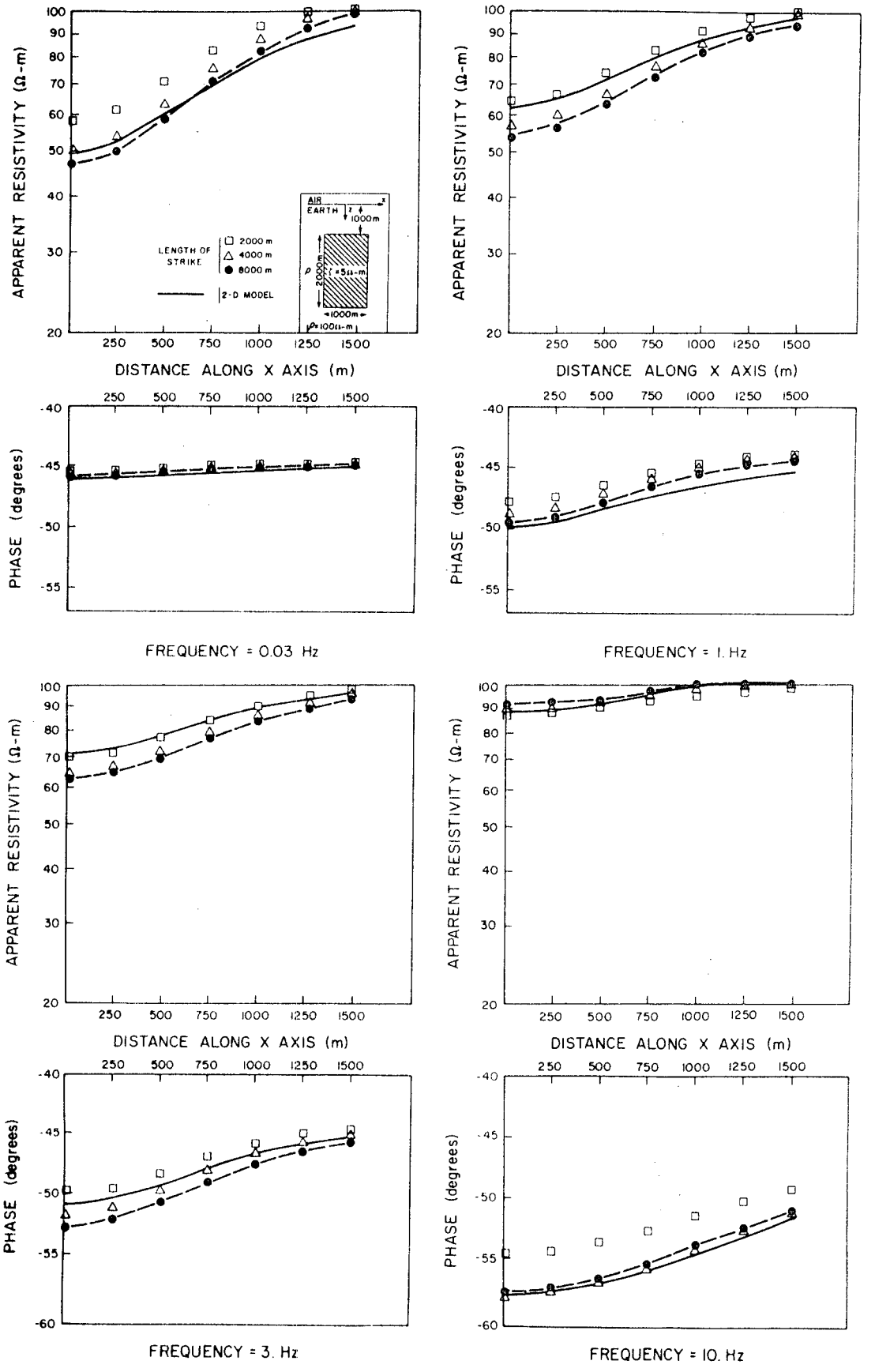

Figure 14. Comparison between 2D results and 3D results for bodies of different length - $E_{\perp}$ excitation.

COMPARISON WITH A LAYERED MODEL

To examine the validity of 1D interpretation over a 3D body, we compared theoretical apparent resistivity for a layered model with results for 3D slabs of different lateral extents. The comparison is shown in Figure 15 for square slabs 200, 400, 800, and 1200 meters on a side, 100 meters deep, and 200 meters thick. The slab resistivity is 3 ohm-m compared to a background resistivity of 100 ohm-m.

The 3D results may not be very accurate at 300 Hz because the cell size of 100 meters is twice the skin depth in the slab. However, the cell size is less than a skin depth at the other frequencies and, furthermore, is equal to the depth to the top of the slab. Hence the 3D results should be accurate except at 300 Hz.

Figure 15 illustrates the important point that, because of space charges at its boundaries, a 3D slab must be very large for 1D interpretation to apply. In this case the 1D and 3D responses are quite different, particularly at low frequencies, even for a 1200m x 1200m slab at 100 m depth. Results are closer at the higher frequencies as volume currents become more important relative to charge at the boundaries. It is obvious that layered-earth interpretation would yield erroneous results.

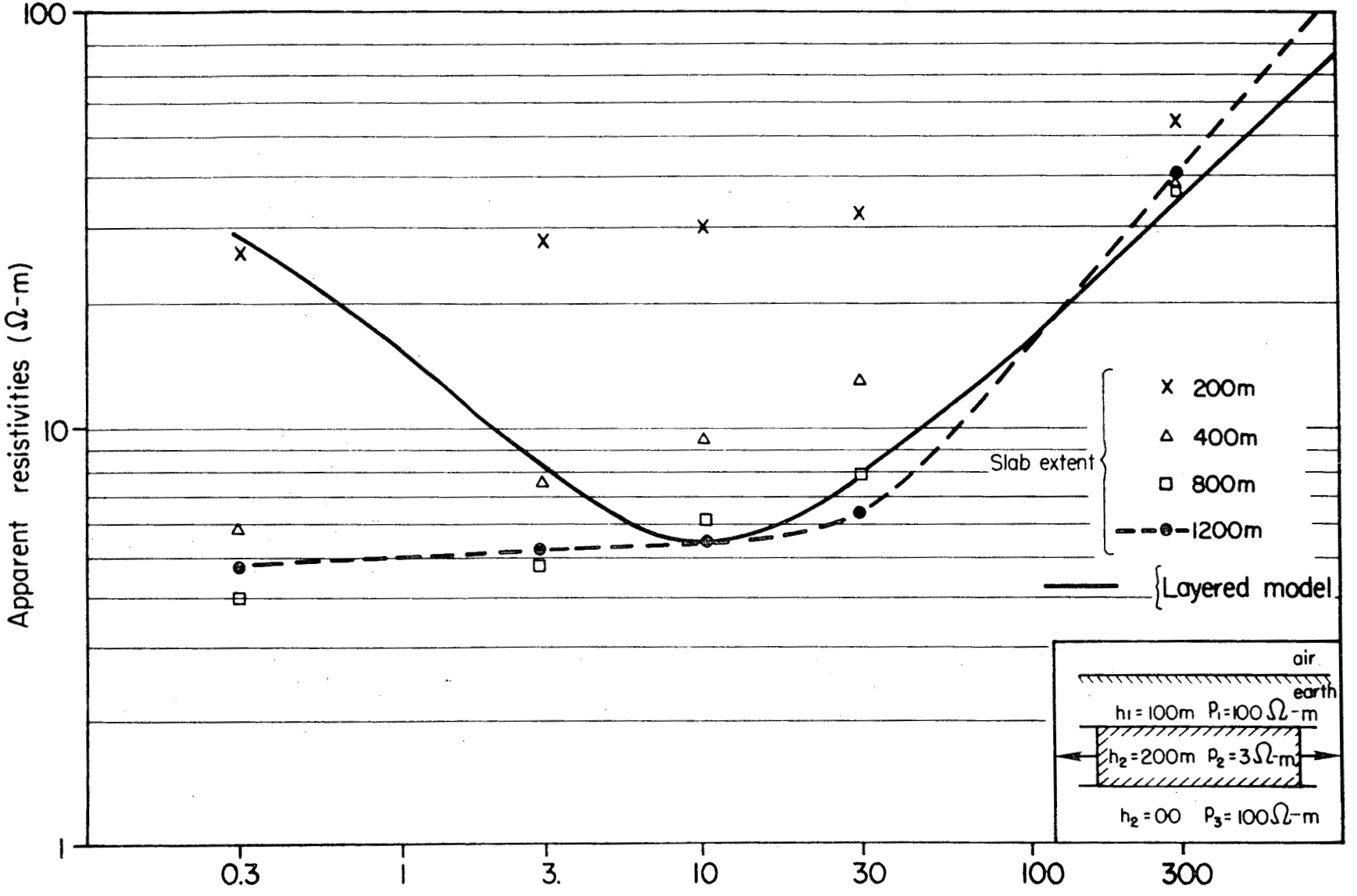

Figure 15. Comparison of results for a layer and for 3D square slabs of different size.

COMPUTATIONS ON A GRID

When the polarization current in an inhomogeneity has been found, the secondary electric and magnetic fields anywhere can be calculated by applying the appropriate dyadic Green's functions (Hohmann, 1975) and integrating over the inhomogeneity. Figures 16-21 show MT results at .03, 1, 3, and 10 Hz on a grid at the earth's surface over the 1 km x 2 km x 2 km conductive body illustrated in Figure 6. The cell size was 250 m for these computations. Because the problem has two planes of symmetry, results are shown for one quadrant only.

Figure 16 shows apparent resistivity, ρ_{yx}, for E_{11} excitation, while ρ_{xy} for $E_{\perp}$ excitation is shown in Figure 17. Because the elongation of the body is not great, resistivity values are similar for the two excitation modes, with the E_{11} case exhibiting slightly lower values. Contours are elongated normal to the incident electric field.

The phase of the impedance $Z_{yx} = E_y/H_x$ is shown in Figure 18 for E_{11}, while the phase of $Z_{xy} = E_x/H_y$ for $E_{\perp}$ is shown in Figure 19. At low frequencies the phase approaches -45 degrees for both incident field orientations, which is the value for a homogeneous earth. The electric field phase increasingly lags the magnetic field phase as the frequency increases, with phase angles being slightly greater for E_{11}. Again, contours are elongated normal to the incident field.

For a 2D model, where the TE and TM modes separate, the vertical magnetic field is associated only with the TE, or E_{11}, mode. Thus it is common in MT

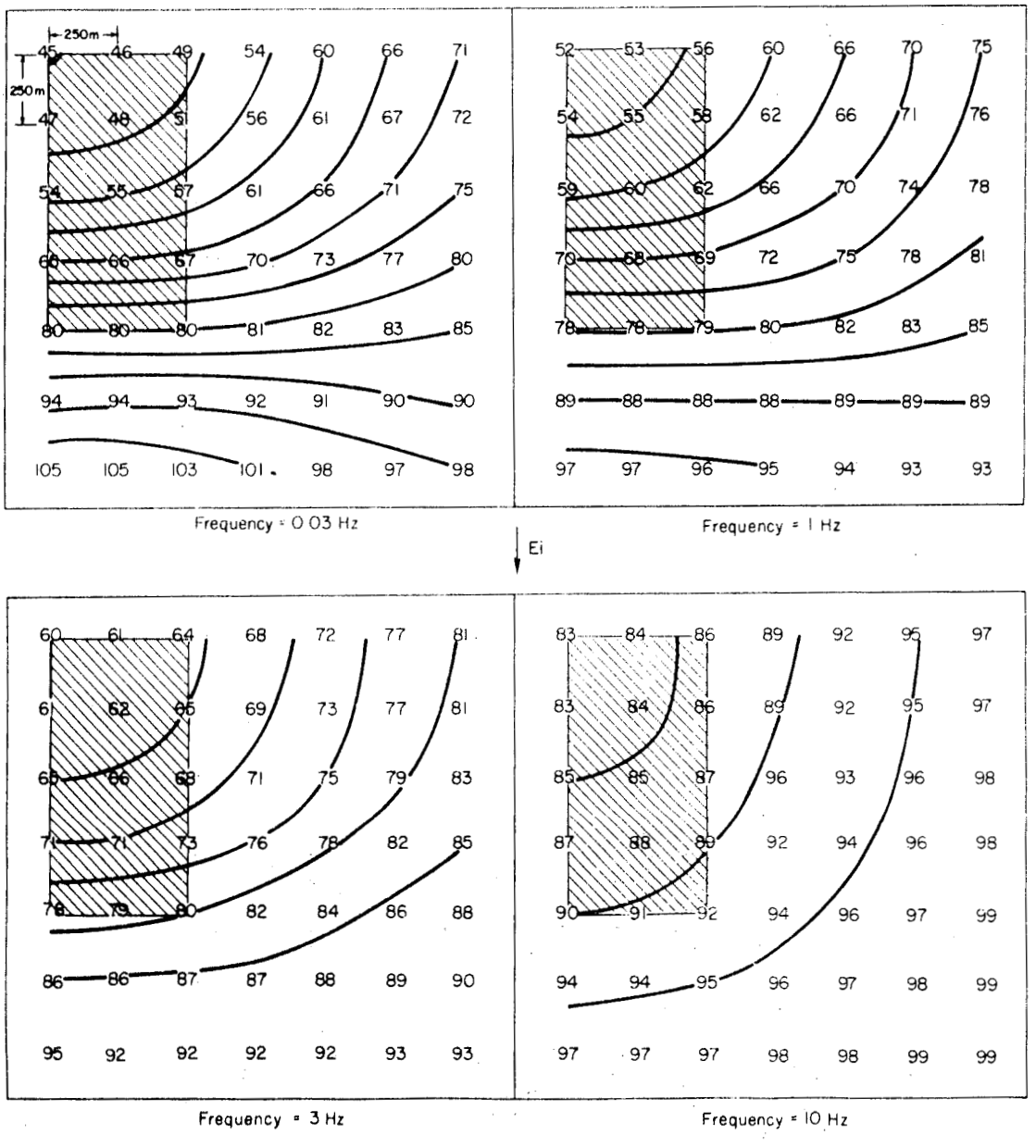

Figure 16. Apparent resistivity on a grid at the surface for the body shown in Figure 6 - E_{11} excitation. Only one quadrant shown.

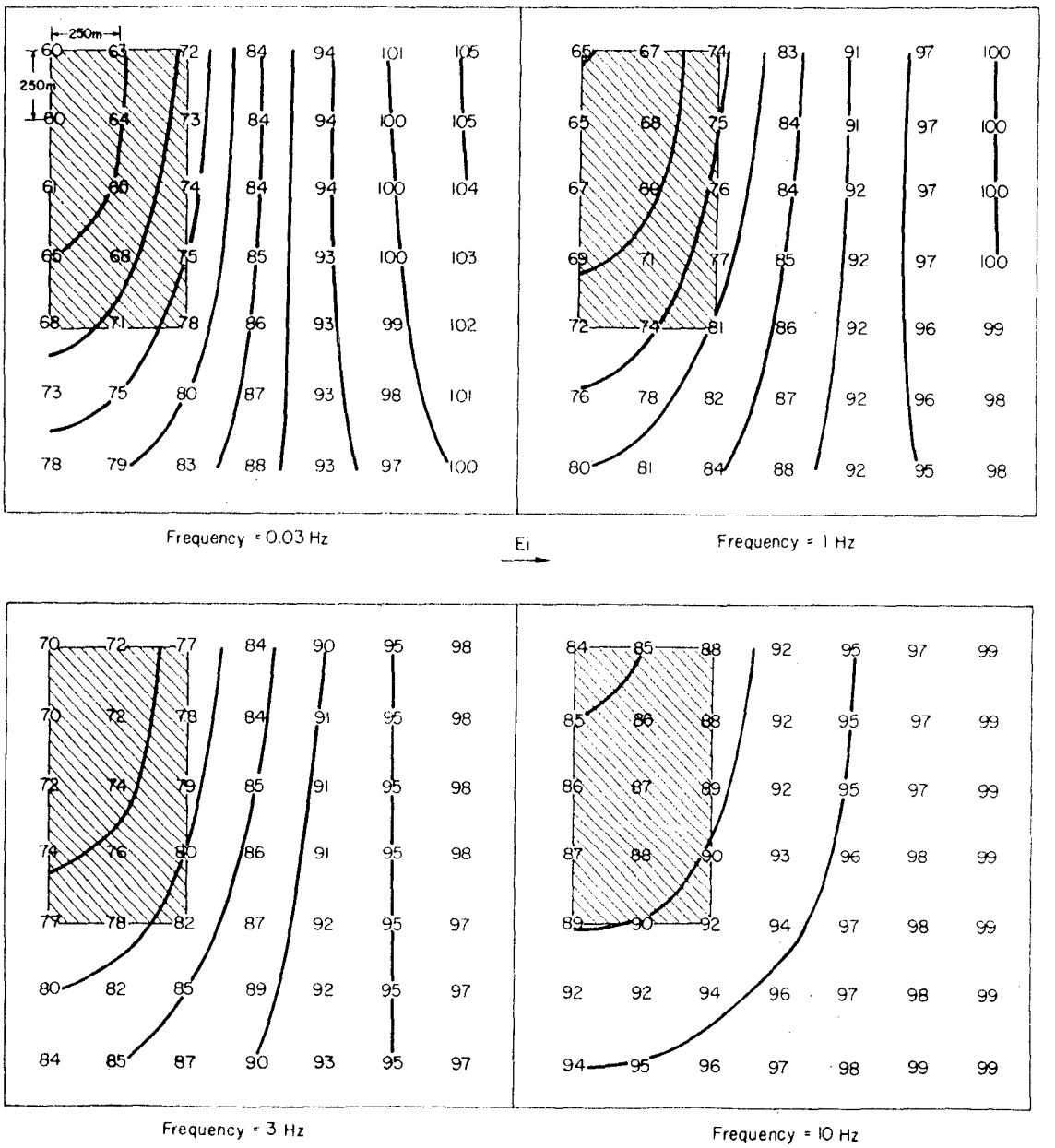

Figure 17. Apparent resistivity on a grid at the surface for the body shown in Figure 6 - $E_{\perp}$ excitation. Only one quadrant shown.

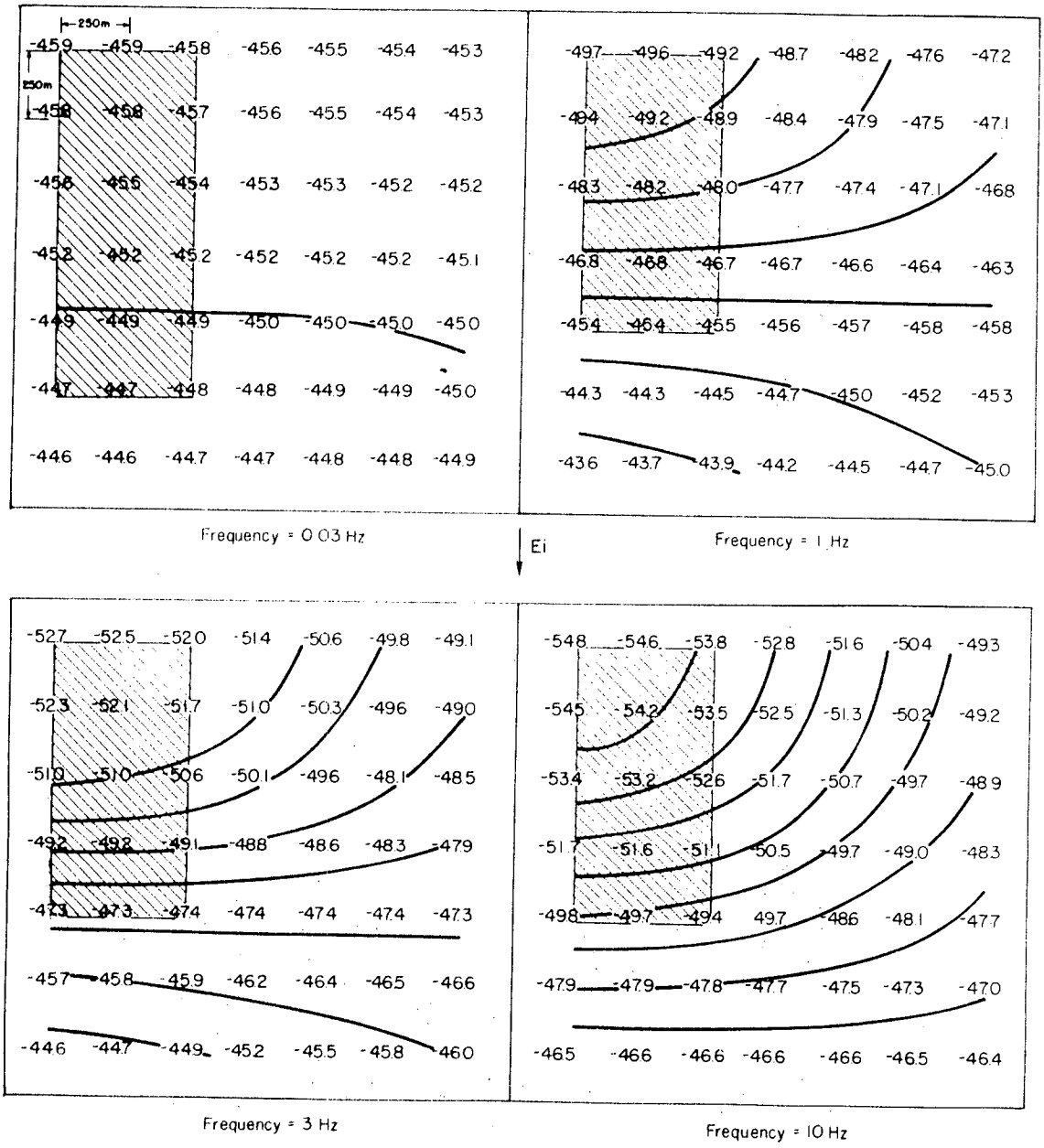

Figure 18. Impedance (Z_{yx}) phase on a grid at the surface for the body shown in Figure 6 - E_{11} excitation. Only one quadrant shown.

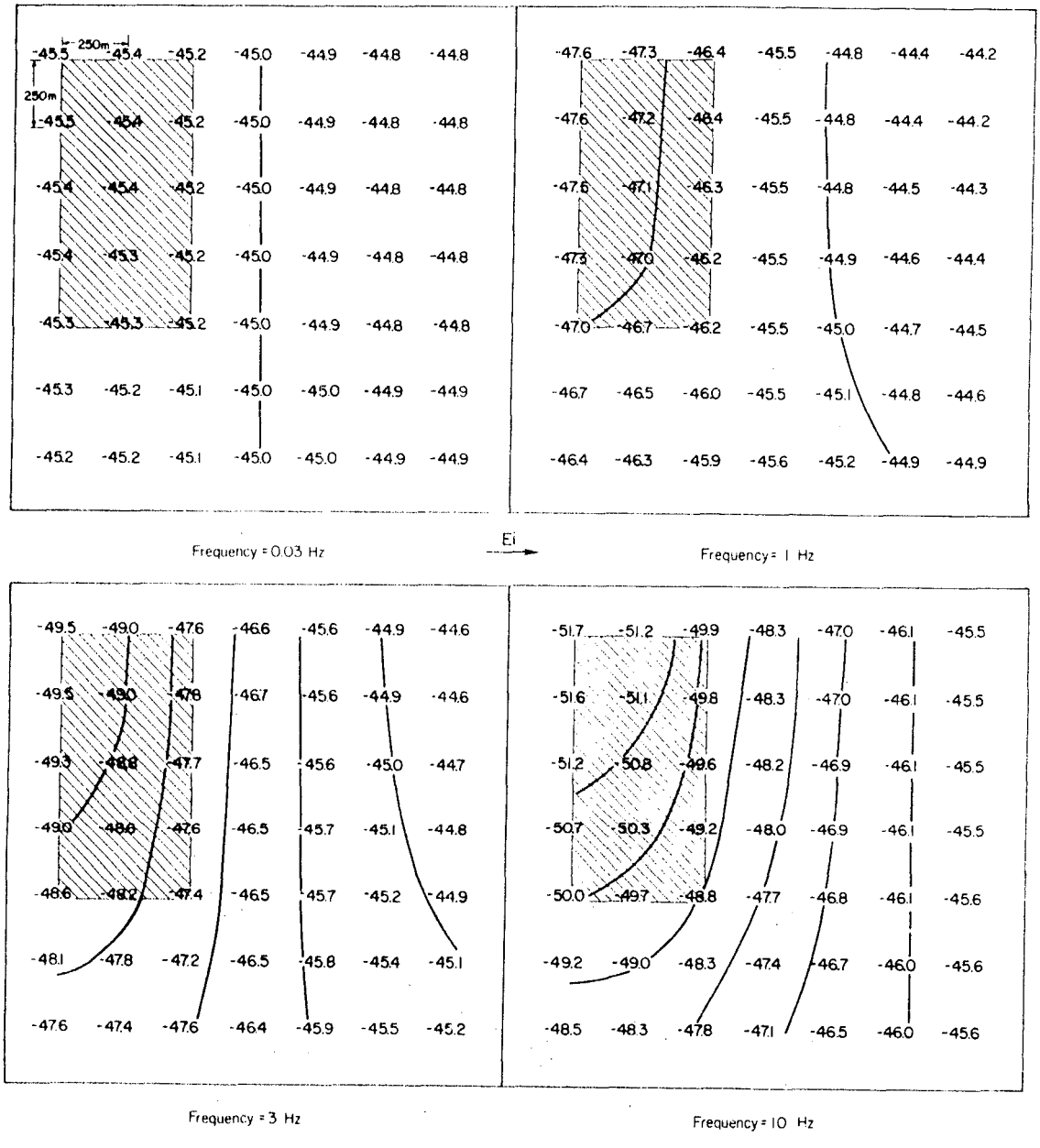

Figure 19. Impedance (Z_{xy}) phase on a grid at the surface for the body shown in Figure 6 - $E_{\perp}$ excitation. Only one quadrant shown.

interpretation to utilize the vertical magnetic field to determine which of the two principal impedance axes is the strike direction, i.e., to identify the modes. The strike direction is taken as normal to that for which the horizontal magnetic field H_x, is most coherent with H_z, the vertical magnetic field.

With our solution, we can calculate H_z at any point over a 3D body for any incident field direction. Figures 20 and 21 show initial results for E_{11} and $E_\perp$ excitation, respectively. The values plotted in Figure 20 are the ratios $|H_z|/|H_x|$ in percent, while those in Figure 21 are for $|H_z|/|H_y|$. Here $|H_x|$ and $|H_y|$ are the amplitudes of the incident fields.

The vertical field is antisymmetric about the yz plane for E_{11} excitation and antisymmetric about the xz plane for $E_\perp$ excitation. Because the TM and TE modes do not separate for a 3D body, $E_\perp$ excitation results in large H_z at many points. This contrasts with the 2D case, where there is no vertical magnetic field for the $E_\perp$ (TM) mode. The vertical magnetic field is larger for E_{11} at the side of the body, while it is larger for $E_\perp$ off the end of the body. Over part of the grid, then, the strike direction would be misinterpreted using conventional procedures.

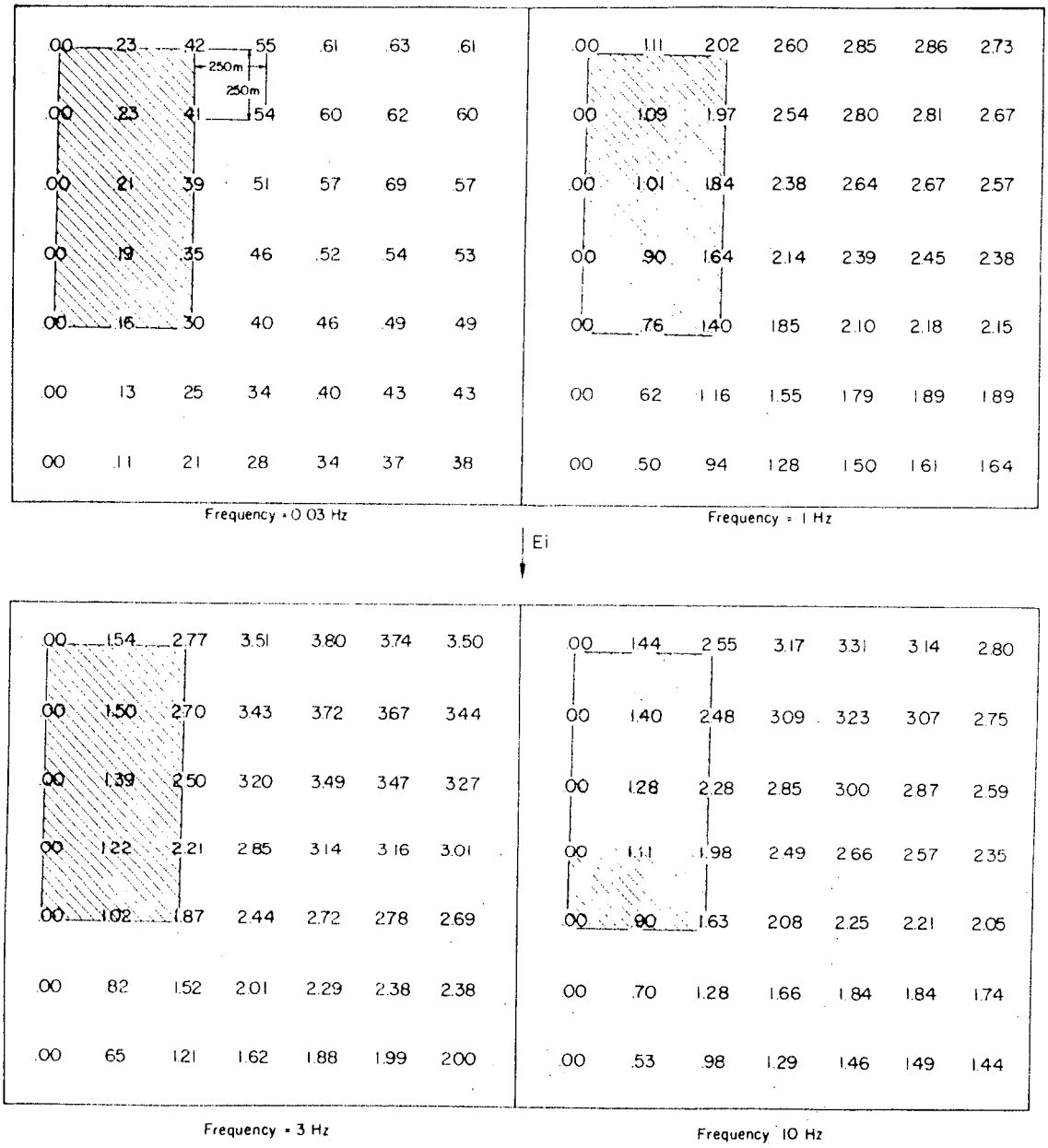

Figure 20. Ratio $|H_z|/|H_x^i|$ in percent on a grid at the surface for the body shown in Figure 6 - E_{11} excitation. Only one quadrant shown.

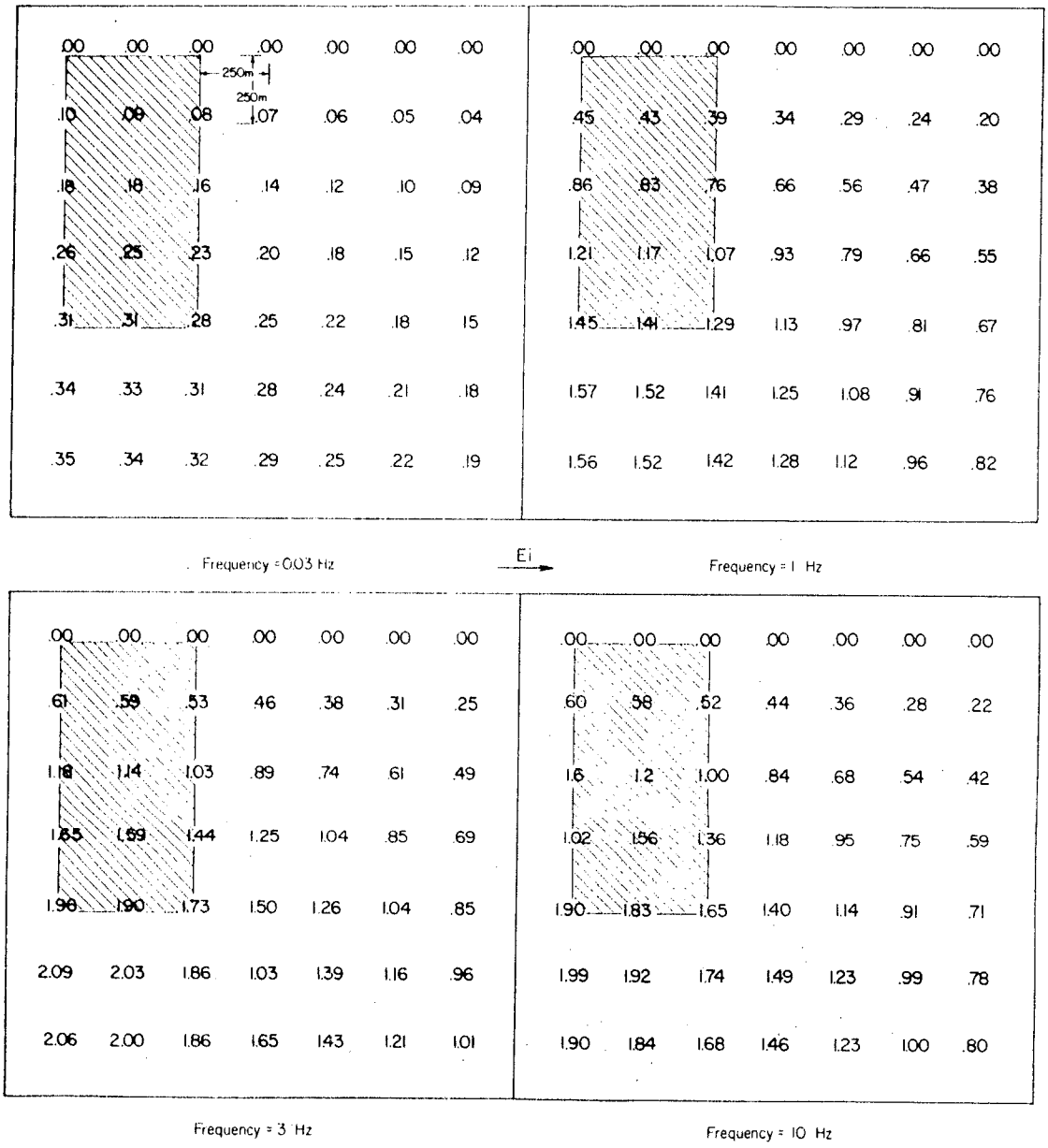

Figure 21. Ratio $|H_z|/|H_y^i|$ in percent on a grid at the surface for the body shown in Figure 6 - $E_\perp$ excitation. Only one quadrant shown.

DISCUSSION

In this report we have documented a new 3D numerical solution for MT analysis and have demonstrated the validity of the results. These initial results also show that 3D models are required for geothermal applications of MT.

We now intend to systematically study MT parameters such as impedance tensor, tipper, skew, etc., in 3D environments, and we will attempt to develop new interpretation techniques. Also we will investigate modifications of the numerical solution for greater accuracy and flexibility.

ACKNOWLEDGEMENTS

This work was funded by the Department of Energy, Division at Geothermal Energy, Contract No. Ey-76-S-07-1601

REFERENCES

Butler, C. M. and Wilton, D. R., 1975, Analysis of various numerical techniques applied to thin-wire scatterers: IEEE Trans. on Ant. & Prop., V AP-23, no. 4, p. 534-540.

Harrington, R. F., 1968, Field computation by moment methods: New York, MacMillan Co.

Hohmann, G. W., 1971, Electromagnetic scattering by two-dimensional conductors in the earth: Ph.D. thesis, Univ. of Calif., Berkeley.

Hohmann, G. W., 1975, Three-dimensional induced polarization and electromagnetic modeling: Geophysics, v. 40, no. 2, p. 309-324.

Jones, F. W., 1974, The perturbation of geomagnetic fields by two-dimensional and three-dimensional conductivity inhomogeneities: Pure & Applied Phys., v. 112, p. 793-800.

Meyer, W. H., 1976, Computer modelling of electromagnetic prospecting methods:

Ph.D. Thesis, Univ. of Calif., Berkeley.

Miller, E. K., and Deadrick, F. J., 1975, Some computational aspects of thin wire modeling in Numerical and asymptotic techniques in electromagnetics; R. Mittra, ed.: New York, Springer-Verlag.

Pridmore, D. F., 1978, Three-dimensional modeling of electric and electromagnetic data using the finite element method: Ph.D. Thesis, Univ. of Utah.

Reddy, I. K., Rankin, D., and Phillips, R. J., 1977, Three-dimensional modeling in magnetotelluric and magnetic variational sounding: Geophys. J. R. Astr. Soc., v. 51, p. 313-325.

Rijo, L., 1977, Modeling of electric and electromagnetic data: Ph.D. Thesis, Univ. of Utah.

Swift, C. M., 1971, Theoretical magnetotelluric and Turam response from two-dimensional inhomogeneities: Geophysics, v. 36, p. 38-52.

Tai, Chen-To, 1971, Dyadic Green's functions in electromagnetic theory: Scranton, International Textbook Co.

Wannamaker, P., 1978, Magnetotelluric investigations at the Roosevelt Hot Springs KGRA and Mineral Mountains, Utah: Univ. of Utah, DOE/DGE Rpt. 78-1701.a.6.1.

Weidelt, P., 1975, Electromagnetic induction in three-dimensional structures. Geophys. J. R. Astr. Soc., v. 41, p. 85-109.

DISTRIBUTION LIST

External

David N. Anderson	Geothermal Resources Council, Davis, CA.
James K. Applegate	Boise State University, Boise, ID.
Carl F. Austin	Geothermal Technology, NWC, China Lake, CA.
Lawrence Axtell	Geothermal Services, Inc., San Diego, CA.
Roger Chapman	California Division of Mines & Geology, Sacramento, CA.
Larry Ball	DOE/DGE, Washington, DC.
Ronald Barr	Earth Power Corporation, Tulsa, OK.
H.C. Bemis	Fluid Energy Corporation, Denver, CO.
Bimal Bhattachryya	USGS, Denver, CO.
David D. Blackwell	Southern Methodist University, Dallas, TX.
Gunnar Bodvarsson	Oregon State University, Corvallis, OR.
C.M. Bonar	Atlantic Richfield Co., Dallas, TX.
David Boore	Stanford University, Stanford, CA.
Francis Bostick	University of Texas, Austin, TX.
Roger L. Bowers	Hunt Energy Corporation, Dallas, TX.
A.J. Brinker	Al-Aquitaine Exploration, Ltd., Denver, CO.
William D. Brumbaugh	Conoco, Ponca City, OK.
Larry Burdge	EG&G Idaho, Idaho Falls, ID.
David Butler	Micro Geophysics Inc., Golden, CO.
David Butler	Chevron Oil Co., San Francisco, CO.
Glen Campbell	Gulf Min. Resource Company, Denver, CO.
David S. Chapman	University of Utah, Salt Lake City, UT.
Bob Christiansen	USGS, Menlo Park, CA.
Jim Combs	Geothermal Services, Inc., San Diego, CA.
F. Dale Corman	O'Brien Resources, Inc., Kentfield, CA.
Ritchie Coryell	National Science Foundation, Washington, DC.
R. Corwin	University of California, Berkeley, CA.
John K. Costain	Virginia Polytechnic Institute, Blacksburg, VA.
James Cotter	DOE/NV, Las Vegas, NV.
Gary Crosby	Phillips Petroleum Company, Del Mar, CA.
K. R. Davis	Thermal Power Company, San Francisco, CA.
Edward Decker	University of Wyoming, Laramie, WY.
William Dolan	Amax Exploration Inc., Denver, CO.
Richard F. Dondanville	Union Oil Co., Santa Rosa, CA.
Earth Sciences Division Library	Lawrence Berkeley Laboratory, Berkeley, CA.
Wilf Elders	University of California, Riverside, CA.
M.C. Erskine, Jr.	Eureka Resource Associates, Berkeley, CA.
A. J. Farstad	Westinghouse Georesearch, Boulder, CO.
Robert T. Forest	Phillips Petroleum Company, Reno, NV.
Frank Frischknecht	U.S. Geological Survey, Denver, CO.
N.E. Goldstein	Lawrence Berkeley Laboratory, Berkeley, CA.
Sidney Green	Terra Tek, Salt Lake City, UT.
Bob Greider	Intercontinental Energy Co., Denver, CO.
John Griffith	DOE/ID, Idaho Falls, ID.

J.H. Hafenbrack	Exxon Co. USA, Denver, CO.
W.R. Hahman	Arizona Bureau of Geology & Mineral Technology Tucson, AZ.
Dee C. Hansen	Utah State Engineer, Salt Lake City, UT.
V. Nobel Harbinson	O'Brien Resources, Incorporated, Toronto, Ontario, Canada.
Norman Harthill	Group Seven, Incorporated, Golden, CO.
Charles E. Helsley	Hawaii Institute of Geophysics, Honolulu, HI.
John F. Hermance	Brown University, Providence, RI.
Margaret E. Hinkle	USGS-Exploration Research, Golden, CO.
George Hopkins	Geotronics Corp., Austin, TX.
Alan Q. Howard	University of Arizona, Tucson, AZ.
Don Hull	Oregon Dept. of Geology & Mineral Industries, Portland, OR.
Gerald W. Huttrer	Intercontinental Energy Corporation, Englewood, CO.
William F. Isherwood	USGS, Menlo Park, CA.
Dallas Jackson	USGS, Hilo, HI.
Jimmy J. Jacobson	Battelle Pacific Northwest Labs., Richland, WA.
George R. Jiracek	University of New Mexico, Albuquerque, NM.
Richard L. Jodry	Richardson, TX
Lewis J. Katz	Utah Geophysical, Incorporated, Salt Lake City, UT.
Paul Kasameyer	Lawrence Livermore Laboratory, Livermore, CA.
George Keller	Colorado School of Mines, Golden, CO.
Paul Kintzinger	Los Alamos Scientific Laboratory, Jemez Springs, NM.
James B. Koenig	Geothermex, Berkeley, CA.
Mark Landisman	University of Texas, Dallas, Richardson, TX.
Art Lange	AMAX Exploration, Incorporated, Denver, CO.
A.W. Laughlin	Los Alamos Scientific Laboratory, Los Alamos, NM.
R.C. Lenzer	Phillips Petroleum Company, Del Mar, CA.
Paul Lienau	OIT, Klamath Falls, OR.
Don R. Mabey	USGS, Denver, CO.
Ted Madden	M.I.T., Cambridge, MA.
Skip Matlick	Republic Geothermal, Santa Fe Springs, CA.
Aldo Mazella	Terra Physics, Richmond, CA.
Robert B. McEuen	Woodward Clyde Consultants, San Francisco, CA.
Don C. McMillan	Utah Geological & Mineral Survey, Salt Lake City, UT.
J.R. McNitt	Energy and Mineral Development Branch, United Nations, NY.
Tsvi Meidav	Consultant, Berkeley, CA.
Jim Mercer	USGS, Reston, VA.
Frank G. Metcalfe	Geothermal Power Corporation, Novato, CA.
John Mitchell	Idaho Dept. of Water Resources, Boise, ID.
Paul Morgan	New Mexico State University, Las Cruces, NM.
Frank Morrison	University of California, Berkeley, CA.
L.J. Patrick Muffler	USGS, Menlo Park, CA.

Misac Nabighian	Newmont Mining Co., Tucson, AZ.
Clayton Nichols	DOE/DGE, Washington, DC.
Denis Norton	University of Arizona, Tucson, AZ.
D. P. O'Brien	QEB, Hayward, CA.
Gary Olhoeft	USGS, Denver, CO.
Carel Otte	Union Oil Company, Los Angeles, CA.
Richard H. Pearl	Colorado Geological Survey, Denver, CO.
Wayne Peeples	Southern Methodist University, Dallas, TX.
Roger Phillips	Jet Propulsion Lab., Pasadena, CA.
Don Pridmore	University of California, Berkeley, CA.
Alan O. Ramo	Sunoco Energy Development Company, Dallas, TX.
Marshall Reiter	New Mexico Institute of Mining & Technology, Socorro, NM.
Robert W. Rex	Republic Geothermal, Inc., Santa Fe Springs, CA.
William L. Rodi	Systems, Science and Software, Inc., LaJolla, CA.
Jack Salisbury	DOE/DGE, Washington, DC.
Robert San Martin	New Mexico Energy Institute, Las Cruces, NM.
Konosuke Sato	Metal Mining Agency of Japan, Minato-Ku, Tokyo.
Wayne Shaw	Getty Oil Company, Bakersfield, CA.
William Sill	University of Utah, Salt Lake City, UT.
H.W. Smith	University of Texas, Austin, TX.
Donald D. Snyder	EDCON, Denver, CO.
John Sonderegger	Montana Bureau of Mines & Geology, Butte, MT.
W. D. Stanley	USGS, Denver, CO.
Neil Stefanides	Union Oil Company, Los Angeles, CA.
John S. Sumner	University of Arizona, Tucson, AZ.
Chandler Swanberg	New Mexico State University, Las Cruces, NM.
Charles M. Swift, Jr.	Chevron Oil Company, San Francisco, CA.
Robert L. Tabbert	Atlantic Richfield Company, Dallas, TX.
Ronald Toms	DOE/DGE, Washington, DC.
Dennis T. Trexler	Nevada Bureau of Mines & Geology, Reno, NV.
John Tsiaperas	Shell Oil Company, Houston, TX.
Donald L. Turner	University of Alaska, Fairbanks, AK.
John Walker	DOE/DGE, Washington, DC.
D. Roger Wall	Aminoil USA, Inc., Santa Rosa, CA.
Gordon West	University of Toronto, Toronto, Canada.
Maggie Widmayer	DOE/ID, Idaho Falls, ID.
David Williams	DOE/DGE, Washington, DC.
Paul Witherspoon	Lawrence Berkeley Laboratory, Berkeley, CA.
B.J. Wynat	Occidental Geothermal, Inc., Bakersfield, CA.
S.H. Yungul	Chevron Resources Company, San Francisco, CA.
K. Zonge	Zonge Engineering & Research, Tucson, AZ.

Internal

S.H. Ward (2)	UU/GG, Salt Lake City, UT.
P.M. Wright	ESL/UURI, Salt Lake City, UT.
W. Ursenbach	UURI, Salt Lake City, UT.
H.P. Ross	ESL/UURI, Salt Lake City, UT.
R.C. Fox	ESL/UURI, Salt Lake City, UT.
W.E. Glenn	ESL/UURI, Salt Lake City, UT.
T.J. Killpack	ESL/UURI, Salt Lake City, UT.
Master Report File	ESL/UURI, Salt Lake City, UT.